



Hay, R., Dung, N.T., Lesimple, A., Unluer, C. and Celik, K. (2021)
Mechanical and microstructural changes in reactive magnesium oxide
cement-based concrete mixes subjected to high temperatures. *Cement and
Concrete Composites*, 118, 103955.
(doi: [10.1016/j.cemconcomp.2021.103955](https://doi.org/10.1016/j.cemconcomp.2021.103955))

There may be differences between this version and the published version.
You are advised to consult the publisher's version if you wish to cite from
it.

<http://eprints.gla.ac.uk/234449/>

Deposited on 18 February 2021

Enlighten – Research publications by members of the University of Glasgow
<http://eprints.gla.ac.uk>

1 **Mechanical and microstructural changes in reactive magnesium oxide cement-based**
2 **concrete mixes subjected to high temperatures**

3
4 R. Hay^a, N.T. Dung^b, A. Lesimple^a, C. Unluer^b, K. Celik^{a*}

5
6 ^aDivision of Engineering, New York University Abu Dhabi, Abu Dhabi, United Arab
7 Emirates

8
9 ^bSchool of Civil and Environmental Engineering, Nanyang Technological University,
10 50 Nanyang Avenue, Singapore 639798

11
12 * Corresponding author. Tel.: +97126287325, E-mail address: kemal.celik@nyu.edu

13
14
15 **Abstract**

16
17 This study investigated the mechanical and microstructural changes in reactive MgO cement-
18 based concrete cured under ambient and accelerated carbonation conditions, followed by
19 exposure to high temperatures. The compressive strength of ambient-cured samples increased
20 from 10 to 30 MPa when subjected to up to 200 °C, which was achieved via increased hydration
21 of the **remaining** MgO. The accelerated formation of brucite at 50 °C enhanced the compressive
22 strength of carbonated samples (58 vs. 65 MPa). A relatively stable performance (~56 MPa)
23 was observed at temperatures ranging between 100 and 300 °C for the carbonated samples,
24 associated with the additional formation of brucite and the transition of nesquehonite and
25 hydromagnesite to artinite. The hydrated magnesium carbonates (HMCs) forming around
26 brucite acted as barriers and inhibited its dehydroxylation. The decomposition of brucite and
27 HMCs at 400 °C caused a porous microstructure and a low residual strength (5-8 MPa) in both
28 the ambient-cured and carbonated samples.

29
30 **Keywords:** Temperature; Microstructure; Carbonation; Stability; MgO; Reactive magnesium
31 oxide cement

32
33 **1 Introduction**

34

35 In search of binders that are relatively more environmentally friendly than Portland cement
36 (PC), researchers have identified reactive magnesium oxide (MgO) cement (RMC) as a
37 promising candidate. The environmental benefits of the material include its ability to absorb
38 and store atmospheric carbon dioxide (CO₂) permanently, its lower production temperatures
39 (i.e., 700-1000 vs. 1450 °C for PC) [1-5], and a possibility for full recyclability [6]. The limited
40 global reserves of MgCO₃, which is used as the raw material to form RMC through calcination,
41 could be overcome with seawater or reject brine from desalination as magnesium-rich sources
42 in the production. In the process, alkali reagents such as lime, calcium hydroxide, dolime
43 (CaO.MgO) [7, 8], hydrated lime (Ca(OH)₂·2H₂O) [9], sodium hydroxide (NaOH) [10, 11],
44 and ammonia solution (NH₄OH) [12] are generally used to increase the pH of the feed solution
45 and thus induce the precipitation of brucite (Mg(OH)₂). The precipitate can be separated by
46 filtering and washing [7] and subsequently calcined to form MgO [11]. In comparison to the
47 utilization of MgCO₃ as the raw material, the waste brine route would potentially help to offset
48 the high embodied CO₂ content [13], of which 1.1 tonnes of CO₂ per unit tonne of MgO arises
49 from the decomposition of MgCO₃ alone [14].

50

51 In addition to the sustainability consideration, one of the main engineering criteria for any
52 material to be applied in construction is its ability to achieve the required mechanical
53 properties. RMC-based composites gain strength through both hydration and carbonation
54 processes. In the hydration process, MgO is converted into Mg(OH)_{2(aq,s)} which provides a
55 limited binding action for the matrix. The formation of Mg(OH)_{2(aq,s)} is also associated with
56 the release of OH⁻ ions and the increase in pH value of the pore solution, thus stimulating
57 the dissolution of CO₂. The dissolved CO₂ reacts with Mg(OH)_{2(aq,s)} to form stable hydrated
58 magnesium carbonates (HMCs) during the carbonation process. Needle-like nesquehonite
59 (MgCO₃·3H₂O), disk/rosette-like hydromagnesite (4MgCO₃·Mg(OH)₂·4H₂O), dypingite
60 (4MgCO₃·Mg(OH)₂·5H₂O), and acicular artinite (MgCO₃·Mg(OH)₂·3H₂O) are the most
61 common HMCs formed in carbonated RMC concrete formulations [3, 4, 15]. The HMCs
62 increase the matrix density as a result of their expansive nature and interconnected networks to
63 promote the binding ability and the associated strength gain of RMC-based composites [16-
64 19]. Thus, the degree of hydration and carbonation are the main factors in determining the
65 performance of RMC samples.

66

67 Significant improvement in the performance of RMC-based composites has been achieved via
68 the enhancement of the hydration and carbonation processes. The classical ball milling method

69 was used to modify the morphology and microstructure of reactive MgO, leading to an
70 improved hydration reaction rate [20]. With the same water-binder ratio of 0.6, the use of
71 hydrochloric acid (HCl) as a hydration agent (HA) at a concentration of 0.05 M enhanced the
72 hydration rate of MgO and formation of $\text{Mg}(\text{OH})_{2(\text{aq},\text{s})}$, resulting in an approximately two-fold
73 increase in the 28-day compressive strength in comparison to a reference mix without the HA
74 [21]. Similarly, the use of magnesium acetate $((\text{CH}_3\text{COO})_2\text{Mg})$ at 0.05 M concentration in
75 RMC-based concrete mixes of a water-binder ratio of 0.55 was responsible for an increase in
76 the hydration degree of MgO by 30% and in the compressive strength by 2.7 times after 14
77 days of curing [17]. Incorporation of nucleation seeding such as hydromagnesite was shown to
78 accelerate the hydration of MgO and induce the formation of an amorphous carbonation phase
79 to contribute to a significant strength enhancement of the composite [22]. By adding 3 wt. %
80 of caustic magnesium oxide and chemical admixture to the RMC, 3D printing of complex
81 structures with precise shape retention were achieved [23].

82

83 Carbonation via elevated CO_2 concentrations (i.e., 5-20%) stimulated the formation of HMCs
84 and resulted in an increase of approximately 7 times in the 28-day compressive strength with
85 respect to ambient carbonation [16, 17, 21, 24]. Moreover, the simultaneous implementation
86 of the hydration agents and the accelerated carbonation increased the 28-day compressive
87 strength by 14 times compared with the control RMC samples cured under the ambient
88 condition (4 MPa vs. 56 MPa) [17]. Under a carbonation environment of 10% CO_2 ,
89 simultaneous inclusion of $(\text{CH}_3\text{COO})_2\text{Mg}$ as a hydration agent and hydromagnesite as seeds
90 improved the hydration and carbonation to result in a 64% improvement in CO_2 sequestration
91 and a 46% increase in the 28-day compressive strength (48 MPa vs. 70 MPa) [18]. The HA or
92 seeds alone led to a strength enhancement of only 42% and 33%, respectively, suggesting a
93 synergy when the two techniques are implemented together. The significant enhancement in
94 the mechanical performance within RMC samples with hydration agents and/or nucleation
95 seeding under the accelerated carbonation was fundamentally attributed to an increase in the
96 carbonation content and formation of HMCs of larger morphologies [5, 17, 18, 21, 25].
97 Supercritical CO_2 (scCO_2) was recently shown to lead to a mature strength development of
98 RMC-based composites within hours of exposure and enhance the CO_2 sequestration content
99 [26]. XRD phase quantification with Rietveld refinement showed that the HMCs were
100 predominantly composed of nesquehonite and hydromagnesite under prolonged carbonation
101 [27]. An investigation with SEM, transmission electron microscopy (TEM), electron energy-
102 loss spectroscopy (EELS), and Raman spectroscopy also indicated the formation of an

103 amorphous phase containing Mg, O, H, and C under both ambient and concentrated CO₂ curing
104 [22, 28].

105

106 With the compressive strength ranging from 10 to 70 MPa [17, 18, 29], RMC-based concrete
107 is applicable in various areas where PC is currently used. Yet, the integrity of the composites
108 under fire or high-temperature exposure has not been explored. Such understanding is critical
109 and would contribute to possible design recommendations as the material gains traction in the
110 construction industry. Indeed, every building material is vulnerable to fire hazards in a real-
111 time environment. Therefore, its stability under high temperatures is vital not only to the overall
112 structural integrity but also to the safety of the occupants of the structures. In this context, the
113 fire resistance of PC-based concrete has been extensively studied [30-32]. Due to the lower
114 thermal conductivity of concrete [33] and its ability to retain a considerable proportion of
115 strength at high temperatures (200-400 °C) [34, 35], international building codes have
116 traditionally set up guidelines for fire protection of structural components by specifying
117 minimum concrete covers to protect the embedded reinforcement [36, 37]. On the other hand,
118 the thermal decomposition of hydration and carbonation products such as nesquehonite,
119 hydromagnesite, and brucite inherent in RMC-based concrete, were individually studied
120 previously [38-41]. The loss of physically bound water from the HMCs occurs in the
121 temperature range of 50-300 °C, whereas the dehydroxylation of brucite and HMCs takes place
122 at nearly 300-500 °C, while the decarbonation starts at about 440 °C. The high thermal
123 decomposition temperature, non-toxicity, and high specific heat make Mg(OH)₂ an attractive
124 fire retardant additive for both polymers and natural fibers composites [42-44]. However, the
125 thermal decomposition of brucite with and without the presence of HMCs as a composite has
126 not been thoroughly investigated, not to mention its thermo-mechanical property evolution,
127 relevance, and implications for building applications.

128

129 This study aims to assess the thermal stability of RMC-based concrete at elevated temperatures
130 (50-400 °C) as specified in building code requirements [45, 46]. A comprehensive investigation
131 was performed on RMC-based composites to provide new insights into the influence of high-
132 temperature exposure on their mechanical and physicochemical properties. A focus was made
133 on the evolution of the micro-mechanical, compressive strength, porosity, morphological and
134 crystal properties of the hydration and carbonation phases. Concrete samples prepared with a
135 hydration agent were cured under ambient and accelerated carbonation conditions. The thermal
136 stability of the concrete was first assessed by its residual compressive strength and

137 microstructural changes after exposure to the elevated temperatures followed by cooling to
138 room temperature. Porosity as an indicator of matrix densification and strength gain was then
139 quantified with mercury intrusion porosimetry (MIP). The morphology evolution of the
140 samples was analyzed by both scanning electron microscopy (SEM) and environmental
141 scanning electron microscopy (ESEM). Meanwhile, the phase transformation was investigated
142 with Fourier-transform infrared spectroscopy (FTIR), X-ray diffraction (XRD),
143 thermogravimetric analysis (TGA), and confocal Raman spectroscopy [47-49]. Finally,
144 nanoindentation, a technique generally used for characterizing the micro-mechanical properties
145 of cement-based materials and their binding phases [50-55], was used to estimate the elastic
146 modulus of the carbonated samples. The indentation results provided signatory elastic modulus
147 data that could be assigned to phases in the composites.

148

149 **2 Materials and Methods**

150

151 **2.1 Materials**

152

153 RMC (commercial name “calcined magnesite 92/200”) used in this study was obtained from
154 Richard Baker Harrison (UK). The physical and chemical properties of RMC are listed in Table
155 1. The reactivity of RMC (i.e., measured by the time required to neutralize 0.25 M of acetic
156 acid by 5 grams of RMC [8]) was recorded as 520 sec. Magnesium acetate ((CH₃COO)₂Mg),
157 obtained from VWR (Singapore), was used as the hydration agent (HA) at a concentration of
158 0.1 M (i.e., based on previous research [17]) to promote the hydration process. Saturated
159 surface dry (SSD) gravel with a particle size of 4.7–9.5 mm was used as the aggregate for
160 preparing the concrete samples.

161

162 **2.2 Sample preparation and methodology**

163

164 Table 2 shows the composition of the prepared concrete samples for this study. The mixture
165 proportion was designed based on the preliminary results and previous studies [5, 18, 21].
166 (CH₃COO)₂Mg 0.1 M solution was used to improve the hydration and carbonation of RMC
167 concrete samples [17, 56]. The ratio of (CH₃COO)₂Mg 0.1 M solution to binder was as high as
168 0.65 to achieve a workable mix due to the high water consumption of RMC as a result of its
169 fine particle size distribution and porous microstructure. Fine aggregates were not included in
170 order to enable the extraction of the carbonated paste from the matrix without any

171 contamination and to ensure accurate quantification of the hydration and carbonation phases
172 via XRD and TGA. After mixing, the concrete was cast into $50 \times 50 \times 50 \text{ mm}^3$ cubic molds,
173 consolidated by a vibration table, and leveled by a trowel. After casting, one set of the samples
174 was cured under accelerated carbonation with a CO_2 concentration of 20% (labeled as C20),
175 while the second set was cured under the ambient condition with an average atmospheric CO_2
176 concentration of $\sim 0.04\%$ (labeled as Amb). For both sets, the relative humidity and
177 temperature were maintained at $80 \pm 5\%$ and $30 \pm 1.5 \text{ }^\circ\text{C}$, respectively. All samples were
178 demolded after 24 hours of casting, and, for compression strength measurement, they were
179 exposed to the two curing conditions for up to 28 days to investigate the strength development.

180

181 The effect of high-temperature exposure was evaluated by heating the samples at 14 days to
182 50, 100, 200, 300, and 400 $^\circ\text{C}$ in an oven. A heating rate of 5 $^\circ\text{C}/\text{min}$ was employed to reach
183 the desired temperature. The target temperature was held for 2 hours as per standard fire safety
184 testing procedures for buildings [45, 46, 57]. Once the heating cycle was completed, the
185 samples were cooled down to room temperature at 5 $^\circ\text{C}/\text{min}$. The samples were annotated by
186 C followed by the CO_2 concentration used for curing and T followed by the temperature at
187 which they were heated for the adopted duration. Thus, the C20-T50 represents a sample cured
188 under 20% CO_2 concentration and heated to 50 $^\circ\text{C}$ for 2 hours. All sample sets were prepared
189 in triplicates, and the compression testing was performed. Paste fragments were extracted from
190 the cubes crushed during the strength testing and were stored in isopropanol for at least seven
191 days to stop hydration. The samples were then dried under a vacuum for another three days
192 before use for all analyses that followed.

193

194 **2.2.1 Compressive strength**

195

196 The compressive strength of the concrete sample was measured by uniaxial loading in
197 triplicates at 1, 3, 7, 14, and 28 days. The equipment used for this purpose was a Toni Technik
198 Baustoffprüfsysteme machine, operated at a loading rate of 55 kN/min . The samples exposed
199 to the high-temperature regimes were also tested at 14 days for residual compressive strengths
200 within 24 hours after the heating to prevent further carbonation and carbonation.

201

202 **2.2.2 Porosity**

203

204 The average pore size distribution of the samples was determined using AutoPore IV 9500
205 high-pressure mercury intrusion porosimetry (MIP) system (Micromeritics) with a pressure
206 capacity of up to 413 MPa (60,000 psi). The paste fragments approximately 10 mm in size
207 from selected cubic samples were used to carry out the MIP analysis. The obtained MIP data
208 was significantly scattered, and therefore the ‘locally weighted scatterplot smoothing
209 (Lowess)’ was applied to get a better insight into the average pore size distribution of the
210 samples.

211

212 2.2.3 Microstructural analysis

213

214 Scanning electron microscopy (SEM) was carried out with a Zeiss Evo 50 electron microscope
215 to investigate the morphology evolution of the carbonation products within the prepared
216 samples. Before the SEM analyses, the vacuum dried samples were mounted onto aluminum
217 stubs using double-sided adhesive carbon tape. The whole assembly was subsequently coated
218 with gold to prevent charging. To characterize the morphology, microstructure, and damage
219 progression of the hydration and carbonation products, environmental SEM (ESEM) was
220 performed on the 28-day sample with Quanta FEG 450 equipped with a heating stage. The
221 sample was heated from 25 °C in a stepwise manner to 50, 100, 200, 300, and 400 °C at the
222 rate of 20 °C/min. Before the image acquisition, the sample was held at these target
223 temperatures for 30 minutes to reach equilibrium.

224

225 2.2.4 FTIR

226

227 The Fourier transformed infrared (FTIR) spectra of samples, used to identify functional groups
228 of carbonation phases, were recorded using an FTIR spectrometer (Cary 670, Agilent) fitted
229 with a diamond attenuated total reflectance (ATR) accessory. The samples were crushed into
230 fine powders and deposited directly on to the diamond lens of the spectrometer. The spectra
231 were then collected in the transmission mode with a wavenumber resolution of 1 cm⁻¹. For each
232 sample, 32 scans were recorded and averaged in the range of 800 cm⁻¹ to 1900 cm⁻¹, where the
233 main vibration bands of HMCs were observed.

234

235 2.2.5 XRD and TGA for phase quantification

236

237 Powder X-ray diffraction (PXRD) patterns were recorded via Philips PW 1800 spectrometer
238 using Cu K α radiation ($\lambda = 1.54060 \text{ \AA}$) with a scanning rate of 0.017° per step in a 2θ range of
239 5° to 70° . The internal standard used for quantification purposes was calcium fluoride (CaF $_2$)
240 mixed at a concentration of 2 wt.%. The quantitative phase analysis of the samples was
241 obtained by the reference intensity ratio (RIR) technique [58-60], as described in the existing
242 literature [18, 25].

243

244 Thermogravimetric analysis (TGA) was conducted on Perkin Elmer TGA 4000 equipment in
245 a temperature range from 30 to 950 °C with a heating rate of 10 °C/min under nitrogen flow.
246 To quantify the amount of different phases in each sample, derivative thermogravimetry (DTG)
247 curves were deconvoluted according to the Gaussian area deconvolution method to reveal the
248 area corresponding to the decomposition of each phase.

249

250 **2.2.6 Confocal Raman microscopy**

251

252 Structural characterization of the exterior surfaces of the respective paste samples was
253 performed with Raman spectroscopy. The technique has been successfully used to identify
254 chemical composition and atomic configuration of both anhydrous and hydrated phases of
255 cement [48, 49, 61] and was shown to be sensitive to the carbon-oxygen (C-O) vibration bond
256 at local atomic environments [62]. The features made it a good candidate to evaluate the
257 prevalence of the carbonation phase in the RMC composites. The Raman spectra were recorded
258 by raster scanning under a confocal Raman microscope, Alpha300 RA from WITec GmbH
259 (Ulm, Germany), equipped with a Zeiss EC Epiplan 20x objective, a 488 nm laser and an
260 SP2300i detector from Princeton Instruments (Acton, MA). The detector had a graze of 600
261 l/mm for scanning in low resolution from 120 to 4000 cm $^{-1}$. Calibration was performed on a
262 silicon wafer using the 520 cm $^{-1}$ emission band prior to sample analysis. The area scanned in
263 confocal Raman mode was 170 by 170 μm with 170 points per line and 170 lines per image
264 under an integration time of 0.2 sec. Data analysis was performed by using the Project 5.0
265 software from Witec. The spectra were first recalibrated by zeroing the position of the Rayleigh
266 band. An average spectrum of the whole scanned area was then obtained, on which the
267 functions of cosmic ray removal, smoothing, and background subtraction were used.

268

269 **2.2.7 Nanoindentation for micro-elastic property characterization**

270

271 Sample fragments whose size ranged between 10-15 mm were embedded in epoxy using 30 ×
272 30 mm cylindrical silicone molds. The **pellet** samples were ground with sandpaper prior to
273 polishing by oil-suspended diamond **bits sequentially** with sizes of 9, 6, 1, and 0.05 μm. The
274 finished surfaces achieved a root-mean-square (RMS) roughness of approximately 100 nm,
275 measured by atomic force microscopy (AFM). Nano-indentation was **then** performed **on the**
276 **polished surface using** a Keysight G-200 Nanoindenter equipped with a diamond Berkovich
277 tip. A programmable technique where the hardness and modulus properties of the material were
278 measured at a specified target penetration depth was adopted [50, 63]. A target penetration
279 depth of 500 nm, about 5 times the surface roughness, was set to achieve an optimum
280 interaction volume larger than the nanogranular globules [64] but smaller than the
281 homogeneous isotropic region of a typical phase [65], thus to achieve repeatable and accurate
282 test data. A surface detection stiffness of 200 N/m and a dwell period of 10 s at the maximum
283 load (to account for thermal drift and creep) were implemented [64, 65]. A total of 64
284 indentations were made in an 8 × 8 matrix at a spacing of 50 μm per region per sample. In a
285 typical indentation experiment, both elastic and plastic deformation occurs during loading, and
286 as a result, the initial unloading branch of the load-displacement curve was used **to quantify the**
287 **elastic modulus**. The elastic modulus (E_p) of the indented material was estimated from Eq. 1.
288 Poisson's ratios of 0.18-0.27, 0.20 and 0.25 were reported for MgO [66], Mg(OH)₂ (MP-30247)
289 and MgCO₃ (MP-5348) [67], respectively. Considering the multi-phase of the hydration and
290 carbonation products in the samples, an **average** Poisson's ratio of 0.24, as adopted by other
291 researchers for hydration products **of Portland cement** [68, 69], was applied in the stiffness
292 calculation. **Though**, it is **important to note** that the second power relationship of Eq. 1 implies
293 that the Poisson's ratio range in between 0.18 to 0.27 would have an **insignificant** effect on the
294 material indentation modulus.

$$295$$
$$296 \quad 1/E_r = (1-\nu^2)/E_p + (1-\nu_i^2)/E_i \quad (1)$$
$$297$$

298 where E_r is the resultant or effective indentation modulus, ν is the Poisson's ratio of the test
299 material, E_i and ν_i are the elastic modulus and Poisson's ratio, respectively, of the indenter. For
300 a diamond tip, $E_i = 1141$ GPa and $\nu_i = 0.07$ [63]. The deconvolution was based on the
301 probability density functions (PDFs) of the tested results plotted with a bin size of 5 GPa.
302 Lorentz distribution was chosen with manually selected initial peak locations. Iterations were
303 subsequently performed to achieve a respective coefficient of determination R^2 greater than
304 0.99.

305

306 3 Results and Discussion

307

308 3.1 Compressive strength and thermal stability

309

310 Fig. 1 (a) shows the compressive strength of RMC samples until 28 days of curing. The samples
311 under the accelerated carbonation condition (C20) exhibited a significant strength
312 development, while the samples under ambient curing (Amb) produced relatively low
313 compressive strength. The accelerated carbonation improved the compressive strength by 5
314 times after 3 days of curing. This proved the important role of carbonation in the strength
315 development of RMC-based concretes. The initial rapid rate of carbonation enabled the C20
316 samples to achieve 51 MPa at 7 days. Afterward, pore reduction with the resulting diffusion
317 control of CO₂ and the precipitation of carbonate phases on uncarbonated Mg(OH)_{2(aq,s)}
318 prevented the progress of the carbonation reaction and reduced the rate of strength gain [26,
319 70]. As a result, C20 samples exhibited a marginal strength gain to 58 MPa at 14 days and 60
320 MPa at 28 days. It is noted that due to diffusion control arising from the matrix densification,
321 the carbonation level was postulated to be non-uniform throughout the sample depth. This was
322 proven in a previous study with X-ray computed tomography based on a correlation between
323 grayscale and sample density [27, 70]. Quantification of the sequestered CO₂ with TGA also
324 confirmed the uneven carbonation where more extensive carbonation was observed for the
325 exterior regions of RMC samples even after prolonged CO₂ exposure [26].

326

327 Fig. 1 (b) presents the residual compressive strength of the RMC samples after being subjected
328 to the high-temperature regimes. The compressive strength of the Amb samples increased from
329 10 MPa to 15 MPa and 30 MPa when subjected to 100 and 200 °C, respectively. This significant
330 increase in the compressive strength could be attributed to dehydration, which improved the
331 cohesion and binding action of brucite, an increase in brucite content under exposure to high
332 temperatures [56], and an improved morphology of the formed brucite. The second mechanism
333 could be a result of the additional conversion of unhydrated MgO to brucite induced by an
334 internal autoclaving condition under the high temperature and the evaporation of water [71,
335 72]. However, the compressive strength of the Amb samples slightly decreased to 25 MPa and
336 then dropped sharply to 5 MPa when subjected to 300 and 400 °C, respectively. The decrease
337 in the compressive strength within this temperature range could be attributed to the

338 dehydroxylation of brucite and decomposition of HMCs. The water loss from the dehydration
339 and dehydroxylation at this high-temperature range can generate high vapor pressure inside the
340 pores, leading to sample spalling [73]. On the other hand, the compressive strength of the C20
341 samples increased to 65 MPa when subjected to 50 °C, then slightly dropped and remained
342 stable at nearly 56 MPa when subjected to temperatures ranging between 100 and 300 °C.
343 However, like the Amb samples, the compressive strength of the C20 samples dropped
344 drastically to 8 MPa when heated further to 400 °C.

345

346 3.2 MIP analysis

347

348 Fig. 2 (a) and (b) show the MIP pore size vs. pore volume distribution of the samples cured
349 under ambient and accelerated carbonation conditions, respectively, followed by exposure to
350 the high temperatures regimes. In the case of the Amb samples, the pore size distribution
351 remained relatively stable with main peaks centered at 0.6 μm up until 100 °C. The large-range
352 pore size for the Amb sample became smaller at 200 °C, attributable to the induced hydration
353 of the remaining MgO. Diffused distribution peaks in size range of 0.01-0.1 μm were observed
354 in all the Amb samples, confirming that smaller pores were also present in minor proportions.
355 When heated further to 400 °C, the Amb-T400 sample showed a significant increase in the
356 number of smaller pores, as indicated by another high-intensity distribution peak at 0.02 μm ,
357 attributable to the thermal decomposition of brucite that occurs at nearly 300 °C.

358

359 As expected, the accelerated carbonation caused an extensive formation of HMCs, which led
360 to significant densification of the microstructure and a reduction in pore sizes. The main peaks
361 occurred at 0.02-0.03 μm for the sample cured under 30 °C. A diffused peak, however, was
362 seen at nearly 0.8 μm , representing a small proportion of larger pores. As compared to the Amb
363 samples, the pore size distribution of the C20 samples was found to be much more sensitive to
364 heat treatment. When heated at 100 °C, the primary distribution peak splits into multiple
365 smaller peaks centered at about 0.02, 0.01, and 0.008 μm . The change was attributed to sample
366 dehydration and likely desorption of water from HMCs, leading to a small decrease in the
367 compressive strength. Heating further to 200 °C and 400 °C induced further formation of
368 smaller pores below 0.005 μm , and larger pores with diffused peaks centered in the range of
369 0.3-0.7 μm were also noted. This resulted in microstructural heterogeneity and a sharp decline
370 in the compressive strength. The large variation in pore size distribution at high temperatures

371 of the RMC samples cured under the accelerated carbonation condition could be closely
372 attributed to the decomposition onset of different HMCs and the loss of physically adsorbed
373 water. Detailed thermodynamic investigations of HMCs [74] revealed that under the ambient
374 pressure, nesquehonite began to dehydrate at temperatures as low as 46 °C and a reversible
375 transformation between the nesquehonite and hydromagnesite could occur at approximately 68
376 °C. On the other hand, the ambient RMC samples displayed greater temperature stability and
377 pore size distribution since they are primarily composed of brucite whose thermal
378 decomposition is initiated at nearly 270 °C.

379

380 3.3 SEM and ESEM

381

382

383

Fig. 3 and

384 Fig. 4 reveal the microstructures of the Amb and the C20 samples subjected to high
385 temperatures after 14 days of curing, respectively. The Amb samples with low carbonate
386 content showed a porous microstructure of tiny platelet brucite with size < 1 μm (

387 Fig. 3 (a)), explaining its low compressive strength. The accelerated hydration, when subjected
388 to 50 °C, resulted in the additional formation of brucite and denser microstructure in the Amb-
389 T50 samples (

390 Fig. 3 (b)). The improvement to the morphology of the hydration products was also achieved
391 when the Amb samples were subjected to 100 °C and 200 °C (

392 Fig. 3 (c) and (d)) with disk-like morphology of brucite observed in the respective samples.

393 The disk-like brucite agglomerated to form a rose-like structure with a diameter of ~1 μm in
394 the Amb-T100 sample and up to ~2μm in the Amb-T200 sample. This development in brucite
395 morphology would contribute to the strength development when the Amb samples were heated
396 up to 200 °C. Agglomerated brucite of an irregular shape with a width of up to ~1 μm was also
397 seen in the Amb-T300 sample (

398 Fig. 3 (e)). Platelet-like brucite started to disappear due to dehydroxylation that occurred at 300
399 °C. Extensive dehydroxylation at 400 °C caused decomposition of brucite flakes, leading to a
400 porous microstructure (

401 Fig. 3 (f)) and the associated strength decline in the Amb-T400 sample relative to the Amb-
402 T200 sample.

403

404 The accelerated carbonation facilitated the formation of HMCs and led to the dense
405 microstructure of the C20 samples after 14 days of carbonation (

406 Fig. 4 (a)). Rosette-like hydromagnesite (~1 µm diameter) formed on top of a solid layer of
407 nesquehonite (~0.5 µm diameter) and provided the filler effect and binding properties in the
408 samples. Cracking was observed on nesquehonite when the C20 samples were subjected to 50
409 °C (

410 Fig. 4 (b)), attributed to its structural instability induced by the loss of bound water at 50 °C
411 [40]. Despite the cracking, there was an increase in the size of nesquehonite as its diameter rose
412 up to 1.2 µm. The improvement in the crystal size, along with the additional formation of
413 brucite as noted in the Amb samples, explained the increase in the compressive strength of the
414 C20-T50 sample when compared with the C20-T30 sample. In the C20-T100 sample,
415 nesquehonite needles were observed to remain interlinked as a dense carbonate phase despite
416 extensive damage to hydromagnesite (

417 Fig. 4 (c)). When the C20 samples were further subjected to 200 °C and 300 °C, nesquehonite
418 seemed to disappear, while hydromagnesite was reduced in size (

419 Fig. 4 (d) and (e)) as also noted in [40]. As the heating proceeded to 400 °C, the dehydroxylation
420 coupled with the decarbonation led to the decomposition of most of the HMCs and brucite,
421 which resulted in the porous microstructure and a sharp strength decline in the C20-T400
422 sample.

423

424 ESEM images for the C20-T30 sample subjected to different heating temperatures are
425 presented in Fig. 5. A focus was made on an area consisting of unreacted MgO (circled) and

426 HMCs, mainly of nesquehonite. Consistent with the SEM observation for the samples under
427 the prolonged heating regimes, cracks in nesquehonite occurred at the temperature of 50 °C
428 due to dehydration, as indicated by an arrow in Fig. 5 (b). However, as the temperature
429 increased, the extent of cracking was noticeably less as compared with the same samples under
430 the prolonged heating. The longer heating duration was postulated to provide more time for
431 dehydration and chemical decomposition of the reaction products, thus resulting in a higher
432 shrinkage and subsequent cracking. The decomposition of HMCs and a corresponding
433 reduction in their unit volumes were observed when the temperature increased from 300 °C to
434 400 °C, as marked by dashed rectangles in Fig. 5 (e) and (f).

435

436 3.4 FTIR

437

438 Fig. 6 (a) and (b) show the FTIR spectra of the samples cured under the ambient and the
439 accelerated carbonation conditions, respectively, and heated to temperatures ranging from 30
440 °C to 400 °C. In the case of the Amb samples heated to 30 °C, 100 °C, and 200 °C, the broad
441 peak centered at 1420 cm⁻¹ and an adjacent diffused shoulder at 1476 cm⁻¹ corresponded to the
442 hydromagnesite and dypingite phases [75]. The presence of nesquehonite could hardly be
443 predicted through a diffuse band at 1648 cm⁻¹, which collectively represented the OH⁻ bending
444 vibration in water present in both the hydromagnesite and nesquehonite phases [76]. However,
445 when the samples were heated to 400 °C, which was above the decomposition temperature
446 (350 °C) of HMCs [77], the peak center shifted to 1458 cm⁻¹ with a diffused shoulder at 1402
447 cm⁻¹, representing the disintegration of HMCs. In the case of the C20 samples heated to 30 °C
448 and 100 °C, the trend was similar except for a new diffused shoulder centered at 1517 cm⁻¹,
449 which was exclusive to the antisymmetric stretching vibration of CO₃²⁻ in the nesquehonite
450 phase with a minor contribution from antisymmetric stretching vibration of CO₃²⁻ in the
451 hydromagnesite phase, as reported in several studies [76, 78]. In addition, the low-intensity
452 bands at 850 and 880 cm⁻¹, corresponding to the bending vibration of CO₃²⁻, collectively
453 represented the hydromagnesite and dypingite phases with a possible existence of the huntite
454 phase [76]. This confirmed that the formation of a variety of HMCs was promoted under the
455 accelerated carbonation, leading to microstructural densification and the associated significant
456 gain strength. At 200 °C, the diffused shoulder at 1517 cm⁻¹ disappeared, showing the
457 instability of the nesquehonite phase. Near the decomposition temperature of HMCs (i.e. at 400
458 °C), the characteristic and broad HMCs peak centered at 1420 cm⁻¹ disappeared and flattened
459 out, which was consistent with a previous high-temperature FTIR study on nesquehonite [78].

460 This thermal decomposition of nesquehonite and other HMCs led to increased porosity and a
461 sharp decline of mechanical properties, as evident in Fig. 1.

462

463 3.5 XRD

464

465 The XRD patterns of samples subjected to the high temperatures after curing under the ambient
466 and the accelerated carbonation are shown in Fig. 7 (a) and (b), respectively. Periclase (MgO;
467 PDF #00-043-1022) and brucite (Mg(OH)₂; PDF #00-007-0239) were observed with the main
468 peaks at 42.9° and 38.1° 2θ, respectively. Dypingite (4MgCO₃·Mg(OH)₂·5H₂O; PDF #00-029-
469 0857), nesquehonite (MgCO₃·3H₂O PDF #00-020-0669), hydromagnesite
470 (4MgCO₃·Mg(OH)₂·4H₂O; PDF #00-025-0513), and artinite (Mg₂CO₃(OH)₂·3H₂O; PDF #00-
471 006-0484) were the main carbonation products observed with the main peaks at 8.1°,
472 13.7°, 15.2°, and 32.8° 2θ, respectively. A comparison of the HMC phases at 14 days before
473 heating (T30) based on the intensity of fluorite (main peak at 28.2° 2θ) as the internal standard
474 revealed higher intensities of HMCs within the samples under the accelerated carbonation
475 curing than the samples under the ambient curing. This higher HMCs content of the carbonated
476 samples was responsible for their higher strength.

477

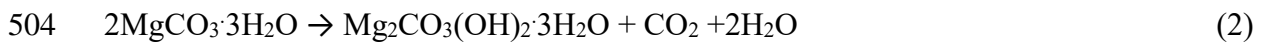
478 As the samples were heated to 50 °C (T50), the brucite content increased in both the samples
479 under the ambient and accelerated carbonation conditions. This increase in brucite content
480 proved the accelerated hydration of MgO under 50 °C. In addition to brucite, the increase in
481 the formation of artinite within the C20 sample was obvious. The formation of artinite could
482 be from the reaction of uncarbonated brucite with ambient CO₂ or dissolved CO₂ in the pore
483 structure. After heating to 50 °C, the Amb samples retained their compressive strength despite
484 the additional formation of brucite, while the C20 sample with the additional formation of
485 brucite and artinite achieved an increase in the compressive strength by 7 MPa. This
486 highlighted the important role of HMC formation in contributing to the strength development
487 of RMC-based concretes.

488

489 As the heating proceeded further, the brucite and artinite contents of the Amb samples
490 increased and were associated with a further increase in the compressive strength until 200 °C.
491 Despite an increase in artinite, the C20 samples exposed to heating experienced an overall
492 loss in the HMCs content and the compressive strength. Their reduction in the HMCs content could
493 be due to the loss of the bound water at around 100 °C to result in a partial collapse of the

494 nesquehonite structure [40, 41]. The brucite content was gradually reduced when the samples
495 were subjected to 300 °C due to its dehydroxylation. This was also associated with the small
496 strength loss in both the Amb and the C20 samples. As the samples were heated to 400 °C, the
497 artinite content decreased in the Amb samples due to its decarbonation, yet significantly rose
498 in the C20 sample. The incline of artinite within the C20 sample could be attributed to its
499 transient phase from the decomposition of other HMCs such as nesquehonite and
500 hydromagnesite as governed by Eq. 2 and 3, respectively. The dehydroxylation and
501 decarbonation after 400 °C led to an increase in the periclase content and the significant
502 strength drop, as previously shown in Fig. 1.

503



505



507

508 The quantification of MgO within each sample is provided in Table 3. It is confirmed that the
509 content of MgO in both the Amb and the C20 samples was reduced up to 200 °C due to its
510 conversion to brucite. At higher temperatures, the MgO content increased as a result of
511 dehydroxylation and decomposition of the HMCs. Also, a reduction in the pore solution pH
512 was found to induce the hydration of MgO [17, 79]. In this study, it is postulated that the
513 dissolution of CO₂ under the accelerated carbonation condition lowered the pore solution pH
514 and consequently improved the hydration of MgO within the C20 samples. This mechanism
515 led to lower unhydrated MgO contents within the samples cured under the accelerated
516 carbonation compared to those cured under the ambient condition.

517

518 3.6 TGA

519

520 The TGA results of the samples subjected to the ambient and accelerated carbonation
521 conditions and followed by exposure to the high temperatures are presented in Fig. 8 (a) and
522 (b), respectively. Without heating, the carbonated samples at 14 days showed a higher mass
523 loss than the corresponding ambient-cured samples. The higher mass loss within the C20
524 samples could be due to the additional decomposition of HMCs. An endothermic peak
525 responsible for the dehydration of water bonded to HMCs was observed at ~100 °C. A strong
526 endothermic peak corresponding to the decomposition of brucite, accompanied by the

527 dehydroxylation (e.g., artinite) and decarbonation (e.g., nesquehonite) of HMCs was observed
528 at around ~360-380 °C. A shoulder peak related to the decarbonation of HMCs was observed
529 at ~440 °C within the C20 samples. Furthermore, two endothermic peaks corresponding to the
530 decarbonation of HMCs were observed at ~540 °C and 600 °C. The samples subjected to higher
531 temperatures (e.g., T300 and T400) had both experienced partial dehydration and
532 dehydroxylation, thereby giving lower mass losses than the samples exposed to lower
533 temperatures (e.g., T30 and T50). The three main decomposition steps of all samples were
534 consistent with the patterns presented in previous studies [38, 40, 80-84] and are summarized
535 below:

536

537 Dehydration of water bonded to HMCs (e.g., artinite, nesquehonite, and dypingite) from 30 °C
538 to 200 °C, as shown in Eq. 4 [40, 80-84]:

539



541

542 Decomposition of uncarbonated brucite (Eq. 5), dehydroxylation of HMCs such as artinite and
543 dypingite (Eq. 6) from 200 °C to 450 °C [40, 81-84]:

544



546



548

549 And decarbonation of residual magnesium carbonate (Eq. 7) from 450 °C to 950 °C [40, 84]:

550



552

553 The mass loss values associated with each of the hydration and carbonation phases obtained by
554 calculating the area of their respective deconvoluted DTG curves are summarized in Table 4.

555 With no high temperatures, all the mass losses would be associated with the dehydroxylation
556 of brucite and HMCs formed during the hydration and carbonation period. The data in Table 4
557 thus represent the decomposition remaining after the high-temperature regimes. It is observed
558 that the mass losses due to the dehydration in the C20 samples were more significant in
559 comparison to the values in the Amb samples. This was attributed to the higher content of

560 HMCs formed during the accelerated carbonation of the C20 samples. According to Table 4,
561 dehydration and dehydroxylation obtained from TGA exhibited a decreasing trend when the
562 samples were heated beyond 200 °C, attributable to partial decomposition of the reaction
563 products under the heat treatment. The decarbonation contents in the Amb sample remained
564 stable until 300 °C, while the decarbonation in the C20 samples noticeably decreased when
565 they were subjected to temperatures greater than 50 °C. In comparison to the Amb samples, the
566 C20 samples subjected to 200-300 °C attained higher dehydroxylation. The finding suggested
567 their higher hydration during the carbonation period and a decreased dehydroxylation rate of
568 brucite due to a physical barrier effect induced by the formation of HMCs.

569

570 An increase in the mass loss due to dehydroxylation was noted in the Amb samples when they
571 were heated to 100 °C (21.5 wt.% at 30 °C vs. 22.6 wt.% at 50 °C and 23.2 wt.% at 100 °C).
572 The result confirmed that the enhanced hydration of the unhydrated MgO to form brucite under
573 the heating regimes. Though, heating at 200 °C reduced the mass loss corresponding to
574 dehydration and dehydroxylation of the Amb sample to 1.4 wt.% and 21.7 wt.%, respectively.
575 Interestingly, the compressive strength of the Amb sample under 200 °C significantly increased
576 when compared to the samples under 100°C (as seen in section 3.1). One possible explanation
577 for the phenomenon is the significant change in morphology of hydration and carbonation
578 products (as shown by SEM), which improved the microstructure and consequently the
579 compressive strength. It is also observed that the mass losses due to dehydration slightly
580 decreased when the heating temperature rose from 200 to 300 °C (1.4 wt.% vs. 1.2 wt.%), while
581 other products were left almost unchanged. This reduction in the dehydration was attributed to
582 the loss of 5 MPa in the compressive strength of the Amb-T300 sample when compared to the
583 Amb-T200 sample. When the heating temperature increased to 400 °C, significant
584 decomposition corresponding to the dehydroxylation and decarbonation occurred. This
585 resulted in the decrease in the total mass loss (27.4 wt.% vs. 19.8 wt.%) and was responsible
586 for a 20 MPa reduction in the compressive strength within the Amb-T400 sample relative to
587 the Amb-T300 samples (25 MPa vs. 5 MPa).

588

589 Similar to the Amb samples, the mass loss corresponding to the dehydroxylation within the
590 C20 samples increased when they were heated up to 100 °C (22.8 wt.% vs. 25.6 wt.%),
591 attributable to the additionally accelerated hydration of the unhydrated MgO. However, the
592 decomposition of HMCs within the C20 samples occurred during the heating, as indicated by
593 the corresponding decrease in the remaining dehydration. For heating from 30 °C to 50 °C, the

594 dehydration decreased from 9.6 wt.% to 9.2 wt.% while the decarbonation was lowered from
595 6.4 wt.% vs. 5.7 wt.%. Despite the decomposition of HMCs and the reduction of total mass
596 loss (38.8 wt.% vs. 37.9 wt.%), the compressive strength of the C20-T50 sample was higher
597 than that of the C20-T30 sample. At 100 °C, the decomposition due to the dehydration and
598 decarbonation was offset by the additional hydration of unhydrated MgO, leading to a similar
599 total mass loss in the C20-T50 sample (37.9 wt.%) and the C20-T100 sample (38 wt.%).
600 However, the loss of 9 MPa in the compressive strength of the C20-T100 indicated the
601 dominant role of the HMCs in dictating the mechanical properties of the composite. At higher
602 temperatures, the C20 samples experienced further decomposition of the hydration and
603 carbonation products. This was reflected by their reduced total mass losses of 33.3 wt.% at 200
604 °C and 31.4 wt.% at 200 °C vs. 38.8 wt.% 100 °C. Though their compressive strengths were
605 of a similar magnitude, and this reinforced the fact that in addition to the content of hydration
606 and carbonation, the morphology played a critical role in strength retention. For the heating of
607 400 °C, the C20-T400 sample retained dehydroxylation of only 13.3 wt.% vs. 23.9 wt.% for
608 the C20-T300. Aggravated by the remaining small dehydration (2.2 wt.%) and decarbonation
609 (4.3 wt.%), the sample underwent a drop of 45 MPa in the compressive strength, as indicated
610 in Fig. 1 (b).

611

612 3.7 Confocal Raman microscopy

613

614 Fig. 9 presents Raman spectra obtained for the external surfaces of the samples under both the
615 ambient and accelerated carbonation conditions and subjected to heating at 30 °C, 50 °C, 200
616 °C, and 400 °C for 2 hours. Normalization was performed with respect to the maximum
617 intensity between Raman shifts of 50 cm⁻¹ and 4000 cm⁻¹. According to Raman spectra obtained
618 from RRUFF database for brucite (R040077), nesquehonite (R050639), hydromagnesite
619 (R060011), dypingite (R070086), and artinite (R060166), the peaks at 277 cm⁻¹, 442 cm⁻¹, 726
620 cm⁻¹, and 1086 cm⁻¹ are attributed to OH⁻ vibration modes in brucite. An additional peak for
621 brucite at 3652 cm⁻¹ was also reported by other researchers [85]. Meanwhile, the peaks in the
622 vicinity of 1100 cm⁻¹ are associated with that of C–O vibration in CO₃²⁻ within carbonation
623 products with slight shifting to the right as compared with the corresponding frequency peak
624 of OH⁻ in brucite. The peak positions from the database are consistent with the Raman spectra
625 presented previously for nesquehonite [80], hydromagnesite [81], and dypingite and artinite
626 [86].

627

628 The Amb samples exposed to heating at 30 °C and 50 °C exhibited peaks at 277 cm⁻¹, 444 cm⁻¹, and 3638 cm⁻¹, associated with OH⁻ vibration due to the presence of Mg(OH)₂ in the matrix
629 system. Heating the Amb samples up to 200 °C did not have a significant effect on the spectrum
630 profile, and this further reinforced the argument that the morphology evolution contributed to
631 strength enhancement of the samples. The decomposition of brucite at temperatures between
632 360 °C and 380 °C led to less intense Raman peaks for the Amb-T400 sample. It is important
633 to note that the application of the background subtraction adopted in data processing resulted
634 in a high noise level and apparent high peaks in the vicinity of 1093 cm⁻¹ and 3646 cm⁻¹, as
635 shown in Fig. 9 (a) for the Amb-T400 sample. Conversely, Fig. 9 (b) revealed that the
636 accelerated carbonation induced the formation of carbonation products, which was evident by
637 peak centers at 1181.1 cm⁻¹ for the C20-T30 and 1118.3 cm⁻¹ for the C20-T50 sample. As
638 compared with the Amb samples, the carbonated samples showed greatly diminished relative
639 intensities in the region of 3638 cm⁻¹ at heating temperatures of 30 °C and 50 °C, indicating a
640 reduced presence of brucite due to its conversion to the carbonation phases. Peaks at low
641 frequency match those of artinite, which was expected to be present as part of the carbonation
642 products. On the other extreme, the spectrum bands in the vicinity of 3416 cm⁻¹ could be
643 assigned to moisture in the system [80]. For the C20-T200 sample, the peak band for moisture
644 became significantly reduced due to dehydration. Also, the peak band in the vicinity of 3638
645 cm⁻¹ for OH⁻ vibration of brucite became more apparent while the peak at 1183 cm⁻¹ became
646 relatively less intense and shifted to 1098 cm⁻¹, attributable to an increase in Mg(OH)₂ content
647 and partial decarbonation of HMCs. Increasing the target heating temperature from 200 °C to
648 400 °C led to greatly reduced peak intensities when compared with those of the C20-T200
649 sample as a result of further dehydroxylation and decarbonation. Nevertheless, the peak at 1098
650 cm⁻¹ assigned to OH⁻ in Mg(OH)₂ persisted. This could be attributed to the presence of HMCs
651 forming layers around brucite and acting as a physical barrier to delay its dehydroxylation.
652

653

654 3.8 Nanoindentation

655

656 Relative frequency plots of elastic modulus data from the nanoindentation experiment are given
657 in Fig. 10 and Fig. 11 for samples cured under the ambient and accelerated carbonation
658 conditions, respectively. The average elastic modulus values for individual nanoindentation
659 tests are also given in Fig. 12. In line with the compressive strength results, it is evident that
660 heating up to 300 °C enhanced the modulus of the Amb samples as marked by a shift of the
661 relative frequency profiles to the right and higher average modulus values as compared with

662 that of the Amb-T30 sample. Interestingly, there is an insignificant difference in the relative
663 frequency plots and the resulting average modulus values for Amb-T100 and Amb-T200 (Fig.
664 10 (c) and (d)). This is consistent with the TGA data, where individual mass losses
665 corresponding to dehydration, dehydroxylation, and decarbonation were very similar among
666 the samples. The onset of decomposition of brucite at a heating temperature of 300 °C led to a
667 slight increase in low modulus phases, as translated into a corresponding reduction in the
668 compressive strength. At 400 °C, the decomposition of brucite led to a more porous
669 microstructure and a significant increase in the low-modulus peak (Fig. 10 (f)).

670

671 When compared with the ambient condition, the accelerated carbonation greatly enhanced
672 micro-mechanical properties of the composite as reflected by a significant increase in the high-
673 modulus phase in the C20-T30 sample (Fig. 11 (a)). Using Lorentz non-linear fit for the sample,
674 the average modulus for HMCs was estimated to be 17.6 GPa. A similar elastic modulus
675 distribution was observed for the C20-T50 and C20-T100 samples (Fig. 11 (b), and (c)), despite
676 a higher compressive strength in the C20-T50 sample. It is anticipated that a possible modulus
677 enhancement, due to improvement in the crystal size of nesquehonite and additional formation
678 of brucite at 50 °C heating, was offset by the nano and micro-crack formation, which was not
679 translated to the overall macro response of the concrete under the compressive testing. Crack
680 propagation in concrete usually initiates from micro defects at the interfacial zones [87], thus
681 obscuring the influence of smaller-scale cracks in the matrix on the overall compressive
682 response. Otherwise, the nano and macro-scale cracks could influence the nanoindentation data
683 due to an interaction micro-volume underneath the indenter tip, whose size was estimated to
684 be approximately 10 times the indentation depth [88, 89] or 5 µm for the case of this study.
685 Consistent with the TGA results where a high level of dehydration of HMCs started to occur
686 at 200 °C, a corresponding reduction in medium modulus (in the range of 17.6 GPa) phases
687 and the associated increase in low modulus phases were observed in the C20-T200, C20-T300,
688 and C20-T400 samples (Fig. 11 (d), (e), and (f)). Despite retaining a higher compressive
689 strength than the Amb-T400 sample, the C20-T400 sample exhibited a higher relative
690 frequency for the low-modulus phases, as also reflected by the lower average modulus value
691 (Fig. 12). The incongruence was attributed to more formation of nano and macro-scale cracking
692 in the C20-T400 sample due to its more intense decomposition at the heating temperature of
693 400 °C.

694

695 4 Conclusions

696

697 With the goal of proving and expanding the potential application areas of reactive MgO cement
698 (RMC) mixes for buildings, this study investigated the strength, composition, and
699 microstructure of RMC-based concrete mixes cured under ambient and accelerated carbonation
700 conditions, followed by exposure to high temperatures ranging from 30 °C to 400 °C. For the
701 ambient-cured samples, the hydration of the remaining MgO was accelerated under heating up
702 to 200 °C. This additional hydration densified the microstructure, which was composed of
703 brucite with an improved morphology. This contributed to significantly higher compressive
704 strengths in the samples (i.e., 10 MPa vs. 30 MPa). At the heating temperatures of 300 °C and
705 400 °C, the dehydroxylation of brucite led to a significant loss of its binding ability. This
706 reduction in brucite was accompanied by an increase in the pore size (i.e., mostly in the range
707 of 0.5-0.7 μm), resulting in a strength decrease to 5 MPa at 400 °C. Consistently, the ambient-
708 cured samples exhibited enhanced micromechanical properties at up to 100 °C. Further
709 exposure to higher temperatures at up to 300 °C did not have a significant influence on their
710 nanoindentation modulus values due to a combined action of crack formation and morphology
711 change.

712

713 For the samples cured under the accelerated carbonation condition, the formation of HMCs not
714 only enhanced the binding ability of the matrix, but also provided a filler effect. This
715 improvement led to a reduction in the pore size, resulting in a significant improvement in their
716 compressive strengths compared with the ambient-cured samples (58 vs. 10 MPa). Exposure
717 to a temperature of 50 °C stimulated the hydration of the remaining MgO to provide an
718 increased amount of brucite. The reaction between dissolved CO₂ and Mg(OH)_{2(aq,s)} improved
719 the morphology of HMCs, which resulted in a further increase in the compressive strength from
720 58 MPa to 65 MPa. Despite the additional formation of brucite at 100-300 °C, the dehydration
721 and decarbonation of HMCs, and the associated cracking led to a slight reduction in the
722 compressive strength of the heated samples from 58 to 56 MPa. The dehydration and
723 decarbonation of HMCs were associated with the transformation of nesquehonite and
724 hydromagnesite to artinite at temperatures of 100-400 °C. The presence of HMCs, forming
725 protective layers around brucite, acted as a physical barrier and decreased its dehydroxylation
726 rate. The strong decarbonation of the carbonated samples at 400 °C led to the loss of HMCs
727 and an increase in the pore size from 0.02-0.03 μm to 0.3-0.7 μm, which resulted in a significant

728 reduction in compressive strength from 58 MPa to 8 MPa as well as the loss of nanoindentation
729 modulus from 17.6 GPa to 2.6 GPa based on frequency plot deconvolution.

730

731 The work contributes to unraveling the mechanical and microstructural performance of
732 composites produced with reactive magnesium oxide cement (RMC) under high temperatures
733 or simulated fire scenarios. Based on the obtained results, it follows that despite the
734 compositional and morphological changes observed at high temperatures, RMC-based
735 composites cured under ambient and accelerated conditions remain mechanically stable
736 without a significant reduction in performance at temperatures as high as 300 °C (i.e. when
737 heated for up to 2 hours at 10 °C/min). These findings highlight the stability of RMC-based
738 concrete under extreme operating conditions. Also, improved fire resistance of the composites
739 may be achieved by including nucleation materials or carbonation agents to preferentially form
740 more stable HMCs. The incorporation of microfibres is also postulated to enhance the structural
741 stability by delaying the cracking initiation within the carbonation products. These topics have
742 been completed [25, 90] or are being investigated by the co-authors.

743

744

745 **Acknowledgments**

746

747 The authors R. Hay and K. Celik thank the NYUAD Center for Interacting Urban Networks
748 (CITIES), funded by Tamkeen under the NYUAD Research Institute Award CG001 and by the
749 Swiss Re Institute under the Quantum Cities™ initiative for providing financial support to
750 make this research possible and wish to express their gratitude to Dr. Abdullah Khalil and Core
751 Technology Platform (CTP) experts, specifically Dr. James Weston and Dr. Liang Li, of New
752 York University Abu Dhabi for their assistance with the experiment and data analyses. The
753 authors N.T. Dung and C. Unluer would like to acknowledge the financial support from the
754 Singapore-MIT Alliance for Research and Technology (SMART) Innovation Centre
755 (ING1510112-ENG (IGN)) for the completion of this research project.

756 **References**

- 757 [1] A.J.W. Harrison, Reactive magnesium oxide cements, Google Patents, United States of
758 America 2008.
- 759 [2] M. Liska, A. Al-Tabbaa, Ultra-green construction: reactive magnesia masonry products,
760 Proceedings of the Institution of Civil Engineers - Waste and Resource Management 162(4)
761 (2009) 185-196.
- 762 [3] M. Liska, A. Al-Tabbaa, K. Carter, J. Fifield, Scaled-up commercial production of
763 reactive magnesium cement pressed masonry units. Part I: Production, Proceedings of the
764 Institution of Civil Engineers-Construction Materials 165(4) (2012) 211-223.
- 765 [4] M. Liska, A. Al-Tabbaa, K. Carter, J. Fifield, Scaled-up commercial production of
766 reactive magnesia cement pressed masonry units. Part II: Performance, Proceedings of the
767 Institution of Civil Engineers-Construction Materials 165(4) (2012) 225-243.
- 768 [5] C. Unluer, A. Al-Tabbaa, Impact of hydrated magnesium carbonate additives on the
769 carbonation of reactive MgO cements, *Cem. Concr. Res.* 54 (2013) 87-97.
- 770 [6] C. Sonat, C.H. Lim, M. Liska, C. Unluer, Recycling and reuse of reactive MgO cements—
771 A feasibility study, *Constr. Build. Mater.* 157 (2017) 172-181.
- 772 [7] H.A. Robinson, R.E. Friedrich, R.S. Spencer, Magnesium hydroxide from sea water,
773 Google Patents, 1946.
- 774 [8] M.A. Shand, The chemistry and technology of magnesia, Wiley Online Library 2006.
- 775 [9] R.H. Dave, P.K. Ghosh, Enrichment of bromine in sea-bittern with recovery of other
776 marine chemicals, *Ind. Eng. Chem. Res.* 44(9) (2005) 2903-2907.
- 777 [10] M. Turek, W. Gnot, Precipitation of magnesium hydroxide from brine, *Ind. Eng. Chem.*
778 *Res.* 34(1) (1995) 244-250.
- 779 [11] H. Dong, C. Unluer, E.-H. Yang, A. Al-Tabbaa, Recovery of reactive MgO from reject
780 brine via the addition of NaOH, *Desalination* 429 (2018) 88-95.
- 781 [12] H. Dong, C. Unluer, E.-H. Yang, A. Al-Tabbaa, Synthesis of reactive MgO from reject
782 brine via the addition of NH₄OH, *Hydrometallurgy* 169 (2017) 165-172.
- 783 [13] W. Shen, L. Cao, Q. Li, Z. Wen, J. Wang, Y. Liu, R. Dong, Y. Tan, R. Chen, Is
784 magnesia cement low carbon? Life cycle carbon footprint comparing with Portland cement, *J.*
785 *Clean. Prod.* 131 (2016) 20-27.
- 786 [14] S. Ruan, C. Unluer, Comparative life cycle assessment of reactive MgO and Portland
787 cement production, *J. Clean. Prod.* 137 (2016) 258-273.
- 788 [15] M. Liska, L.J. Vandeperre, A. Al-Tabbaa, Influence of carbonation on the properties of
789 reactive magnesia cement-based pressed masonry units, *Adv. Cem. Res.* 20(2) (2008) 53-64.
- 790 [16] L. Vandeperre, A. Al-Tabbaa, Accelerated carbonation of reactive MgO cements, *Adv.*
791 *Cem. Res.* 19(2) (2007) 67-79.
- 792 [17] N.T. Dung, C. Unluer, Sequestration of CO₂ in reactive MgO cement-based mixes with
793 enhanced hydration mechanisms, *Constr. Build. Mater.* 143 (2017) 71-82.
- 794 [18] N.T. Dung, C. Unluer, Development of MgO concrete with enhanced hydration and
795 carbonation mechanisms, *Cem. Concr. Res.* 103 (2018) 160-169.
- 796 [19] R. Hay, K. Celik, Hydration, carbonation, strength development and corrosion resistance
797 of reactive MgO cement-based composites, *Cement and Concrete Research* 128 (2020)
798 105941.
- 799 [20] A. Khalil, K. Celik, Optimizing reactivity of light-burned magnesia through mechanical
800 milling, *Ceramics International* 45(17, Part B) (2019) 22821-22828.
- 801 [21] N.T. Dung, C. Unluer, Improving the performance of reactive MgO cement-based
802 concrete mixes, *Constr. Build. Mater.* 126 (2016) 747-758.
- 803 [22] C. Kuenzel, F. Zhang, V. Ferrándiz-Mas, C.R. Cheeseman, E.M. Gartner, The
804 mechanism of hydration of MgO-hydromagnesite blends, *Cem. Concr. Res.* 103 (2018) 123-
805 129.

806 [23] A. Khalil, X. Wang, K. Celik, 3D printable magnesium oxide concrete: towards
807 sustainable modern architecture, *Additive Manufacturing* 33 (2020) 101145.

808 [24] C. Unluer, A. Al-Tabbaa, Enhancing the carbonation of MgO cement porous blocks
809 through improved curing conditions, *Cem. Concr. Res.* 59 (2014) 55-65.

810 [25] N.T. Dung, C. Unluer, Influence of nucleation seeding on the performance of carbonated
811 MgO formulations, *Cem. Concr. Compos.* 83 (2017) 1-9.

812 [26] R. Hay, K. Celik, Accelerated carbonation of reactive magnesium oxide cement (RMC)-
813 based composite with supercritical carbon dioxide (scCO₂), *Journal of Cleaner Production*
814 248 (2020) 119282.

815 [27] N.T. Dung, A. Lesimple, R. Hay, K. Celik, C. Unluer, Formation of carbonate phases
816 and their effect on the performance of reactive MgO cement formulations, *Cement and*
817 *Concrete Research* 125 (2019) 105894.

818 [28] R. Zhang, N. Bassim, D.K. Panesar, Characterization of Mg components in reactive
819 MgO–Portland cement blends during hydration and carbonation, *Journal of CO₂ Utilization*
820 27 (2018) 518-527.

821 [29] N.T. Dung, C. Unluer, Influence of accelerated hydration and carbonation on the
822 performance of reactive magnesium oxide concrete, *Adv. Cem. Res.* (2018) 1-13.

823 [30] V.K.R. Kodur, T.C. Wang, F.P. Cheng, Predicting the fire resistance behaviour of high
824 strength concrete columns, *Cem. Concr. Compos.* 26(2) (2004) 141-153.

825 [31] B. Persson, Fire resistance of self-compacting concrete, SCC, *Mater. Struct.* 37(9)
826 (2004) 575-584.

827 [32] S. Aydın, B. Baradan, Effect of pumice and fly ash incorporation on high temperature
828 resistance of cement based mortars, *Cem. Concr. Res.* 37(6) (2007) 988-995.

829 [33] D. Darwin, C.W. Dolan, A.H. Nilson, *Design of concrete structures*, McGraw-Hill
830 Education 2016.

831 [34] C.-S. Poon, S. Azhar, M. Anson, Y.-L. Wong, Strength and durability recovery of fire-
832 damaged concrete after post-fire-curing, *Cem. Concr. Res.* 31(9) (2001) 1307-1318.

833 [35] M. Li, C. Qian, W. Sun, Mechanical properties of high-strength concrete after fire, *Cem.*
834 *Concr. Res.* 34(6) (2004) 1001-1005.

835 [36] British Standard, Eurocode 2: Design of concrete structures - Part 1-1: General rules and
836 rules for buildings British Standard Institution, London (2004).

837 [37] ACI Committee 318, Building code requirements for structural concrete (ACI 318-08)
838 and commentary ACI Committee 318, 2008.

839 [38] L.A. Hollingbery, T.R. Hull, The thermal decomposition of huntite and
840 hydromagnesite—A review, *Thermochim. Acta* 509(1–2) (2010) 1-11.

841 [39] H. Ren, Z. Chen, Y. Wu, M. Yang, J. Chen, H. Hu, J. Liu, Thermal characterization and
842 kinetic analysis of nesquehonite, hydromagnesite, and brucite, using TG–DTG and DSC
843 techniques, *J. Therm. Anal. Calorim.* 115(2) (2014) 1949-1960.

844 [40] G. Jauffret, J. Morrison, F.P. Glasser, On the thermal decomposition of nesquehonite, *J.*
845 *Therm. Anal. Calorim.* 122(2) (2015) 601-609.

846 [41] J. Lanas, J.I. Alvarez, Dolomitic lime: thermal decomposition of nesquehonite,
847 *Thermochim. Acta* 421(1) (2004) 123-132.

848 [42] S. Miyata, T. Imahashi, H. Anabuki, Fire-retarding polypropylene with magnesium
849 hydroxide, *Journal of Applied Polymer Science* 25(3) (1980) 415-425.

850 [43] M. Sain, S.H. Park, F. Suhara, S. Law, Flame retardant and mechanical properties of
851 natural fibre–PP composites containing magnesium hydroxide, *Polymer degradation and*
852 *stability* 83(2) (2004) 363-367.

853 [44] A. Genovese, R.A. Shanks, Structural and thermal interpretation of the synergy and
854 interactions between the fire retardants magnesium hydroxide and zinc borate, *Polymer*
855 *Degradation and Stability* 92(1) (2007) 2-13.

856 [45] BS 476, Fire tests on building materials and structures, British Standards Institution,
857 London, 2009.

858 [46] ISO 834, Fire resistance test - elements of building construction, International Standard
859 834, Switzerland, 2012.

860 [47] E. Enríquez, M.A. De la Rubia, A. Del Campo, F. Rubio-Marcos, J.F. Fernández,
861 Characterization of Carbon Nanoparticles in Thin-Film Nanocomposites by Confocal Raman
862 Microscopy, *J. Phys. Chem. C*. 118(19) (2014) 10488-10494.

863 [48] M. Torres-Carrasco, A. del Campo, M.A. de la Rubia, E. Reyes, A. Moragues, J.F.
864 Fernández, New insights in weathering analysis of anhydrous cements by using high spectral
865 and spatial resolution Confocal Raman Microscopy, *Cem. Concr. Res.* 100 (2017) 119-128.

866 [49] J. Higl, M. Köhler, M. Lindén, Confocal Raman microscopy as a non-destructive tool to
867 study microstructure of hydrating cementitious materials, *Cem. Concr. Res.* 88 (2016) 136-
868 143.

869 [50] G. Constantinides, F.J. Ulm, K. Van Vliet, On the use of nanoindentation for
870 cementitious materials, *Mater. Struct.* 36(3) (2003) 191-196.

871 [51] J.J. Chen, L. Sorelli, M. Vandamme, F.J. Ulm, G. Chanvillard, A Coupled
872 nanoindentation/SEM-EDS study on low water/cement ratio Portland cement paste: evidence
873 for C-S-H/Ca (OH) 2 nanocomposites, *Am. Ceram. Soc.* 93(5) (2010) 1484-1493.

874 [52] W. Wilson, J.M. Rivera-Torres, L. Sorelli, A. Durán-Herrera, A. Tagnit-Hamou, The
875 micromechanical signature of high-volume natural pozzolan concrete by combined statistical
876 nanoindentation and SEM-EDS analyses, *Cem. Concr. Res.* 91 (2017) 1-12.

877 [53] L. Göbel, C. Bos, R. Schwaiger, A. Flohr, A. Osburg, Micromechanics-based
878 investigation of the elastic properties of polymer-modified cementitious materials using
879 nanoindentation and semi-analytical modeling, *Cem. Concr. Compos.* 88 (2018) 100-114.

880 [54] S. Gautham, S. Sasmal, Recent Advances in Evaluation of intrinsic mechanical
881 properties of cementitious composites using nanoindentation technique, *Constr. Build. Mater.*
882 223 (2019) 883-897.

883 [55] R. Hay, J. Li, K. Celik, Influencing factors on micromechanical properties of calcium
884 (alumino) silicate hydrate C-(A-)S-H under nanoindentation experiment, *Cem. Concr. Res.*
885 134 (2020) 106088.

886 [56] N.T. Dung, C. Unluer, Carbonated MgO concrete with improved performance: The
887 influence of temperature and hydration agent on hydration, carbonation and strength gain,
888 *Cement and Concrete Composites* 82(Supplement C) (2017) 152-164.

889 [57] G.A. Khoury, Effect of fire on concrete and concrete structures, *Progr. Struct. Eng.*
890 *Mater.* 2(4) (2000) 429-447.

891 [58] C.R. Hubbard, R.L. Snyder, RIR-measurement and use in quantitative XRD, *Powder*
892 *Diffraction* 3(02) (1988) 74-77.

893 [59] R.L. Snyder, The use of reference intensity ratios in X-ray quantitative analysis, *Powder*
894 *Diffraction* 7(4) (1992) 186-193.

895 [60] Q. Johnson, R. Zhou, Checking and estimating RIR values, *Advances in X-ray Analysis*
896 42 (2000) 287-296.

897 [61] R. Masmoudi, K. Kupwade-Patil, A. Bumajdad, O. Büyüköztürk, In situ Raman studies
898 on cement paste prepared with natural pozzolanic volcanic ash and Ordinary Portland
899 Cement, *Constr. Build. Mater.* 148 (2017) 444-454.

900 [62] S. Ortaboy, J. Li, G. Geng, R.J. Myers, P.J.M. Monteiro, R. Maboudian, C. Carraro,
901 Effects of CO₂ and temperature on the structure and chemistry of C-(A-) S-H investigated
902 by Raman spectroscopy, *RSC Advances* 7(77) (2017) 48925-48933.

903 [63] Agilent Technologies, Nano Indenter G200, Palo Alto, CA 94304 USA, 2013.

904 [64] G. Constantinides, F.-J. Ulm, The nanogranular nature of C-S-H, *J. Mech. Phys. Solids*
905 55(1) (2007) 64-90.

906 [65] P. Trtik, B. Münch, P. Lura, A critical examination of statistical nanoindentation on
907 model materials and hardened cement pastes based on virtual experiments, *Cem. Concr.*
908 *Compos.* 31(10) (2009) 705-714.

909 [66] C.-S. Zha, H.-k. Mao, R.J. Hemley, Elasticity of MgO and a primary pressure scale to 55
910 GPa, *Proceedings of the National Academy of Sciences* 97(25) (2000) 13494-13499.

911 [67] M. De Jong, W. Chen, T. Angsten, A. Jain, R. Notestine, A. Gamst, M. Sluiter, C.K.
912 Ande, S. Van Der Zwaag, J.J. Plata, Charting the complete elastic properties of inorganic
913 crystalline compounds, *Sci. Data* 2 (2015) 150009.

914 [68] G. Constantinides, F.-J. Ulm, The effect of two types of C-S-H on the elasticity of
915 cement-based materials: Results from nanoindentation and micromechanical modeling, *Cem.*
916 *Concr. Res.* 34(1) (2004) 67-80.

917 [69] C. Hu, Z. Li, A review on the mechanical properties of cement-based materials measured
918 by nanoindentation, *Constr. Build. Mater.* 90 (2015) 80-90.

919 [70] N.T. Dung, R. Hay, A. Lesimple, K. Celik, C. Unluer, Influence of CO₂ concentration
920 on the performance of MgO cement mixes, *Cement and Concrete Composites* 115 (2021)
921 103826.

922 [71] M. Saad, S.A. Abo-El-Enein, G.B. Hanna, M.F. Kotkata, Effect of temperature on
923 physical and mechanical properties of concrete containing silica fume, *Cem. Concr. Res.*
924 26(5) (1996) 669-675.

925 [72] Q. Ma, R. Guo, Z. Zhao, Z. Lin, K. He, Mechanical properties of concrete at high
926 temperature—A review, *Constr. Build. Mater.* 93 (2015) 371-383.

927 [73] M.C.M. Gary R. Consolazio, W.R. Jeff, III, Measurement and Prediction of Pore
928 Pressures in Saturated Cement Mortar Subjected to Radiant Heating, *Mater. J.* 95(5).

929 [74] A.M. Chaka, A.R. Felmy, Ab initio thermodynamic model for magnesium carbonates
930 and hydrates, *J. Phys. Chem. A* 118(35) (2014) 7469-7488.

931 [75] L. Hopkinson, K. Rutt, G. Cressey, The transformation of nesquehonite to
932 hydromagnesite in the system CaO-MgO-H₂O-CO₂: An experimental spectroscopic study, *J.*
933 *Geol.* 116(4) (2008) 387-400.

934 [76] L. Hopkinson, P. Kristova, K. Rutt, G. Cressey, Phase transitions in the system MgO–
935 CO₂–H₂O during CO₂ degassing of Mg-bearing solutions, *Geochim. Cosmochim. Acta* 76
936 (2012) 1-13.

937 [77] R.C. Weast, M.J. Astle, W.H. Beyer, *CRC handbook of chemistry and physics*, CRC
938 Press, Boca Raton FL1989.

939 [78] R.L. Frost, Raman spectroscopic study of the magnesium carbonate mineral
940 hydromagnesite (Mg₅ [(CO₃)₄ (OH)₂] · 4H₂O), *J. Raman Spectrosc.* 42(8) (2011) 1690-
941 1694.

942 [79] K.P. Matabola, E.M. van der Merwe, C.A. Strydom, F.J.W. Labuschagne, The influence
943 of hydrating agents on the hydration of industrial magnesium oxide, *J. Chem. Technol.*
944 *Biotechnol.* 85(12) (2010) 1569-1574.

945 [80] V. Vágvölgyi, R.L. Frost, M. Hales, A. Locke, J. Kristóf, E. Horváth, Controlled rate
946 thermal analysis of hydromagnesite, *J. Therm. Anal. Calorim.* 92(3) (2008) 893-897.

947 [81] R.L. Frost, S.J. Palmer, Infrared and infrared emission spectroscopy of nesquehonite
948 Mg(OH)(HCO₃) · 2H₂O—implications for the formula of nesquehonite, *Spectrochim. Acta A*
949 *Mol. Biomol. Spectrosc.* 78(4) (2011) 1255-1260.

950 [82] S. Purwajanti, L. Zhou, Y. Ahmad Nor, J. Zhang, H. Zhang, X. Huang, C. Yu, Synthesis
951 of magnesium oxide hierarchical microspheres: A dual-functional material for water
952 remediation, *ACS Appl. Mater. Interfaces* 7(38) (2015) 21278-21286.

953 [83] P. Ballirano, C. De Vito, V. Ferrini, S. Mignardi, The thermal behaviour and structural
954 stability of nesquehonite, MgCO₃ · 3H₂O, evaluated by in situ laboratory parallel-beam X-ray

955 powder diffraction: New constraints on CO₂ sequestration within minerals, *J. Hazard. Mater.*
956 178(1–3) (2010) 522-528.

957 [84] R.L. Frost, S. Bahfenne, J. Graham, W.N. Martens, Thermal stability of artinite,
958 dypingite and brugnatellite—Implications for the geosequestration of green house gases,
959 *Thermochim. Acta* 475(1) (2008) 39-43.

960 [85] T.S. Duffy, C. Meade, Y. Fei, H.-K. Mao, R.J. Hemley, High-pressure phase transition
961 in brucite, Mg(OH)₂, *American Mineralogist* 80(3-4) (1995) 222-230.

962 [86] R.L. Frost, S. Bahfenne, J. Graham, Raman spectroscopic study of the magnesium-
963 carbonate minerals—artinite and dypingite, *Journal of Raman Spectroscopy: An International*
964 *Journal for Original Work in all Aspects of Raman Spectroscopy, Including Higher Order*
965 *Processes, and also Brillouin and Rayleigh Scattering* 40(8) (2009) 855-860.

966 [87] P. Mehta, P.J.M. Monteiro, *Concrete: Microstructure, Properties, and Materials*, 3rd ed.,
967 McGraw-Hill Professional 2006.

968 [88] G. Constantinides, K.S.R. Chandran, F.J. Ulm, K.J. Van Vliet, Grid indentation analysis
969 of composite microstructure and mechanics: Principles and validation, *Mater. Sci. Eng. C.*
970 430(1-2) (2006) 189-202.

971 [89] J.J. Chen, L. Sorelli, M. Vandamme, F.J. Ulm, G. Chanvillard, A coupled
972 nanoindentation/SEM-EDS study on low water/cement ratio Portland cement paste: evidence
973 for C–S–H/Ca(OH)₂ nanocomposites, *J. Am. Ceram. Soc.* 93(5) (2010) 1484-1493.

974 [90] N.T. Dung, T.J.N. Hooper, C. Unluer, Improving the carbonation resistance of Na₂CO₃-
975 activated slag mixes via the use of reactive MgO and nucleation seeding, *Cem. Concr.*
976 *Compos.* (2020) 103832.

977

List of Tables

Table 1 Chemical composition and physical properties of RMC.

	Chemical composition (%)							Physical properties	
	MgO	SiO ₂	CaO	R ₂ O ₃	K ₂ O	Na ₂ O	LOI	Specific gravity (g/cm ³)	Specific surface area (m ² /g)
RMC	>91.5	2.0	1.6	1.0	-	-	4.0	3.0	16.3

Table 2 Compositions of RMC-based concrete used in this study.

Solution/RMC	Mix proportion (kg)		
	RMC	Aggregates	(CH ₃ COO) ₂ Mg 0.1M solution
0.65	550.0	1050.0	357.5

Table 3 MgO content within each sample, obtained by XRD.

Sample	MgO (%)	
Amb	T30	54.7
	T50	50.2
	T100	48.7
	T200	49.1
	T300	64.4
	T400	81.7
	C20	T30
T50		35.8
T100		34.2
T200		35.0
T300		59.6
T400		69.5

Table 4 Mass losses of all samples, obtained by TGA.

Sample	Mass loss (wt.%)				
	Dehydration	Dehydroxylation	Decarbonation	Total	
Amb	T30	2.6	21.5	4.7	28.8
	T50	2.4	22.6	4.6	29.6
	T100	1.8	23.2	4.5	29.5
	T200	1.4	21.7	4.6	27.7
	T300	1.2	21.6	4.6	27.4
	T400	1.0	14.7	4.1	19.8
C20	T30	9.6	22.8	6.4	38.8
	T50	9.2	23.0	5.7	37.9
	T100	7.4	25.6	5.0	38.0
	T200	3.9	24.6	4.9	33.3
	T300	2.9	23.9	4.6	31.4
	T400	2.2	13.3	4.3	19.8

List of Figures

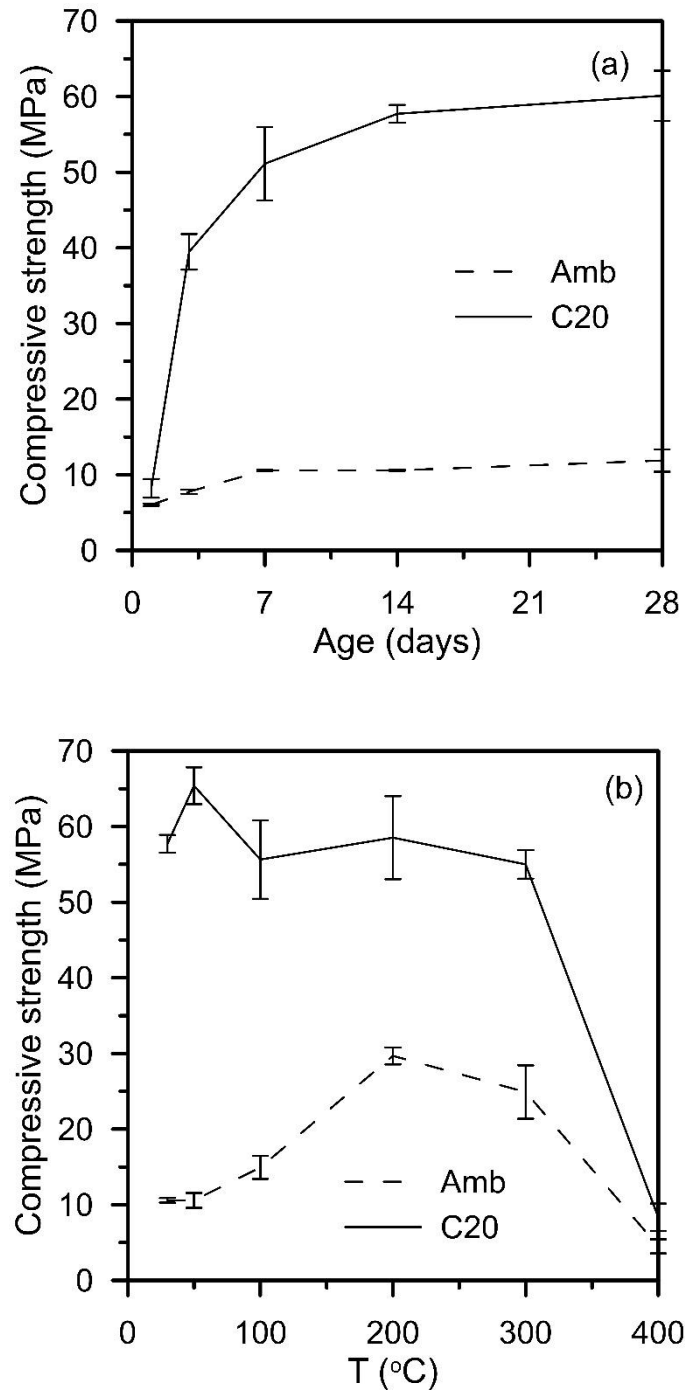


Fig. 1 Compressive strength of concrete samples: (a) cured for up to 28 days and (b) heated for 2 hours after 14 days of curing

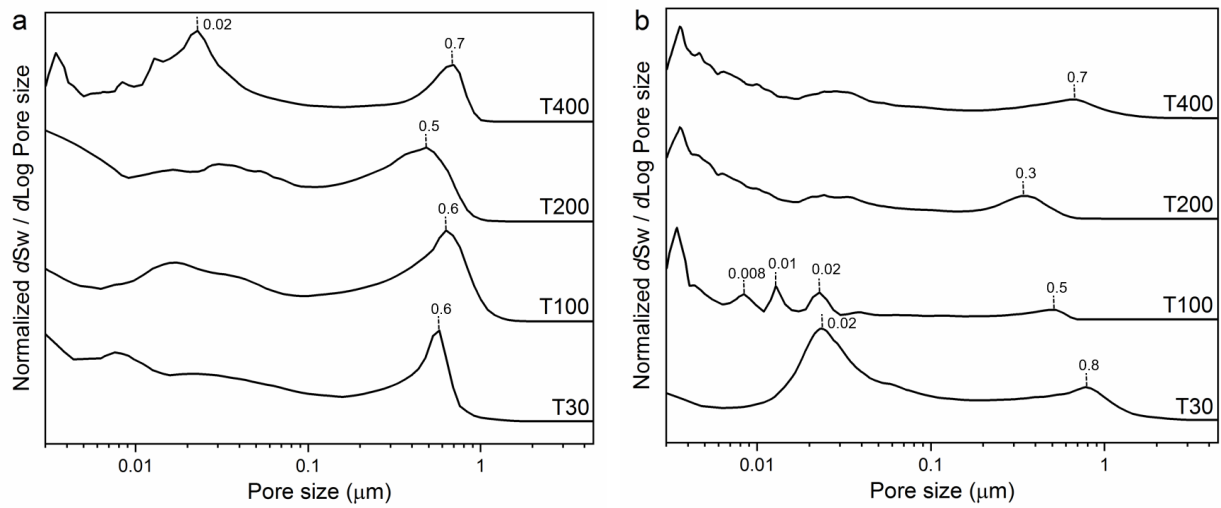


Fig. 2 MIP pore size distribution of samples cured under (a) ambient and (b) accelerated carbonation conditions and heated at different temperatures

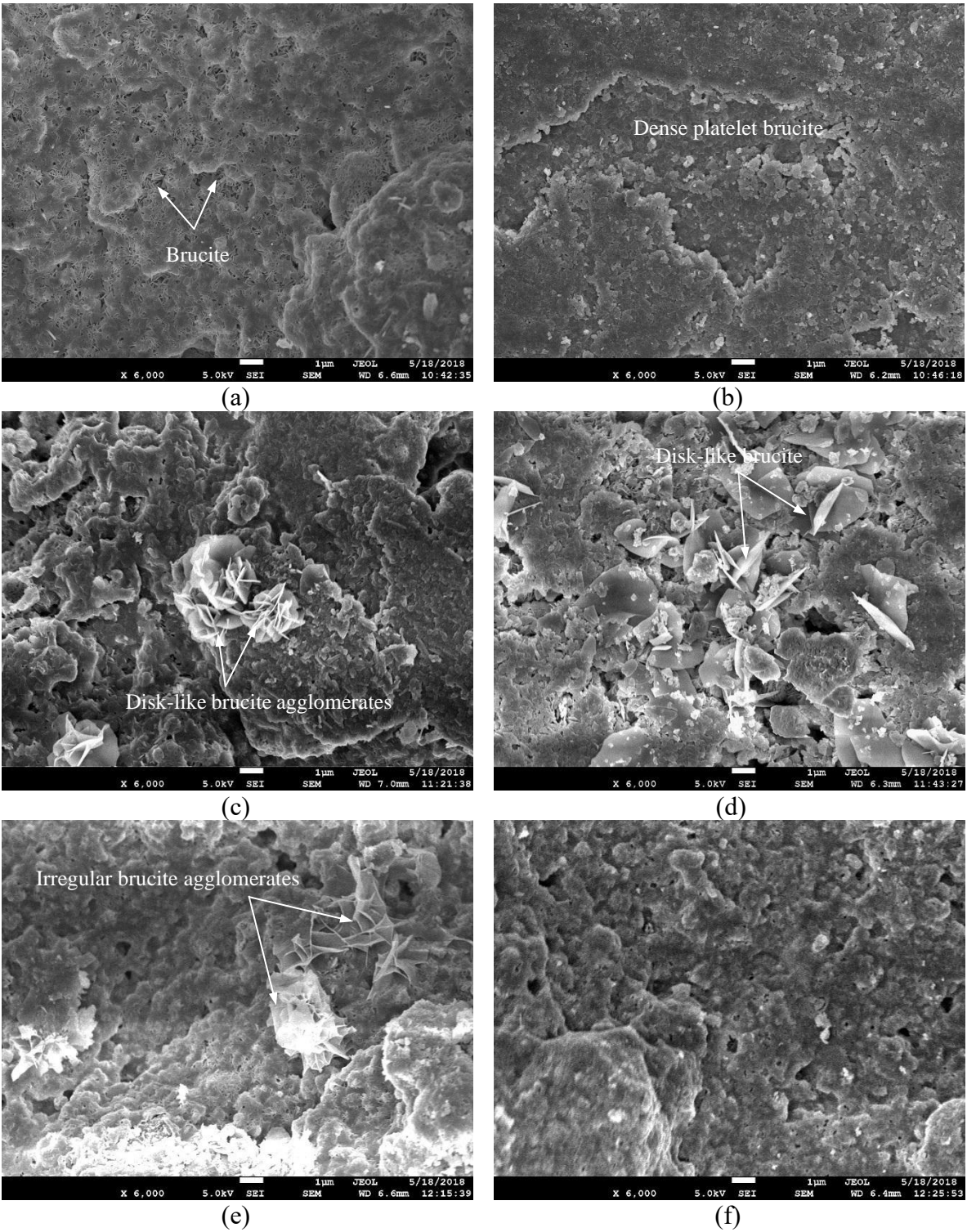
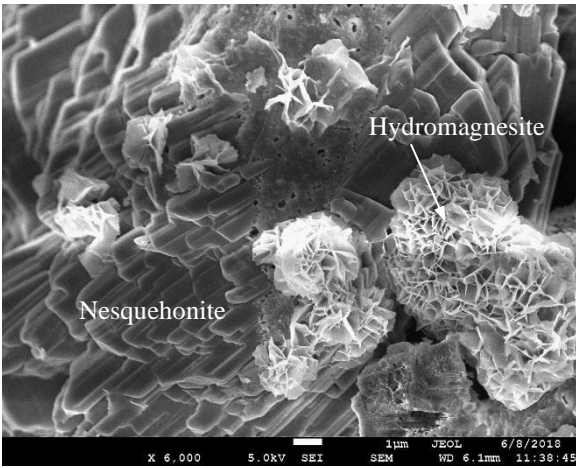
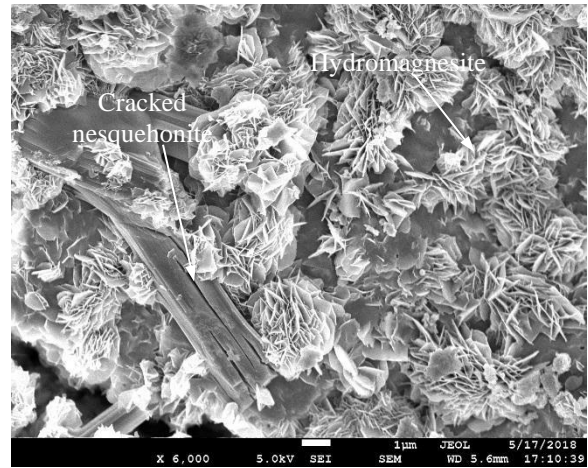


Fig. 3 SEM images of samples after 14 days of ambient curing, followed by an exposure to: (a) 30 °C, (b) 50 °C, (c) 100 °C, (d) 200 °C, (e) 300 °C and (f) 400 °C



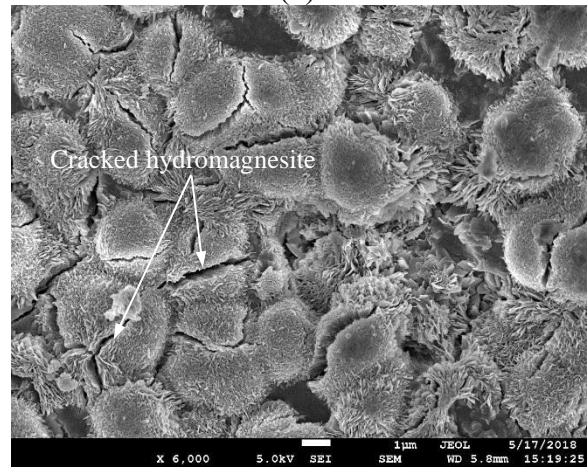
(a)



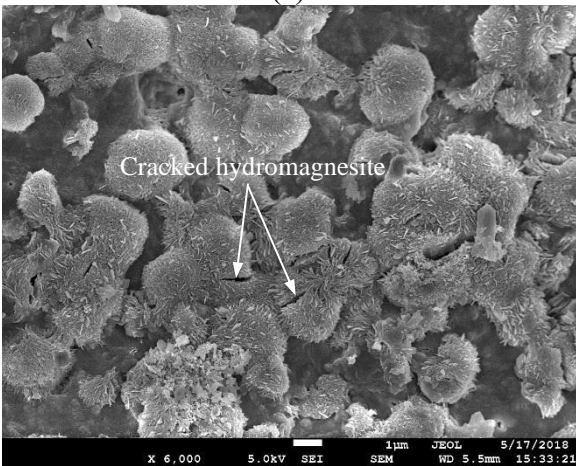
(b)



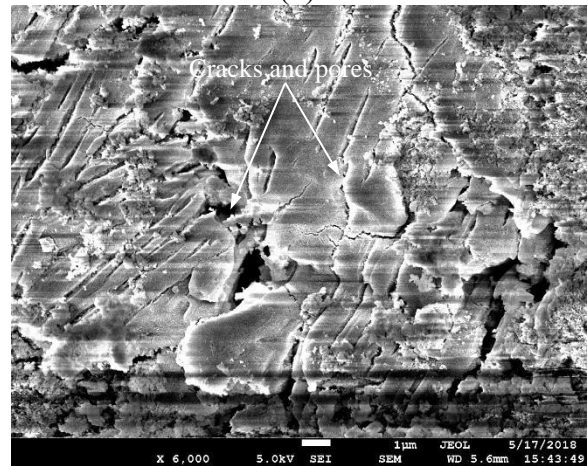
(c)



(d)

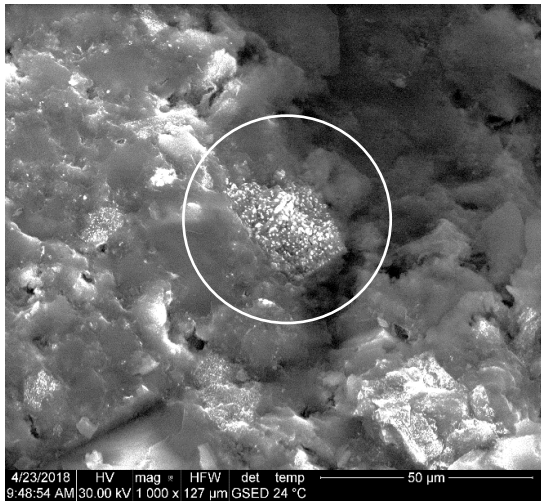


(e)

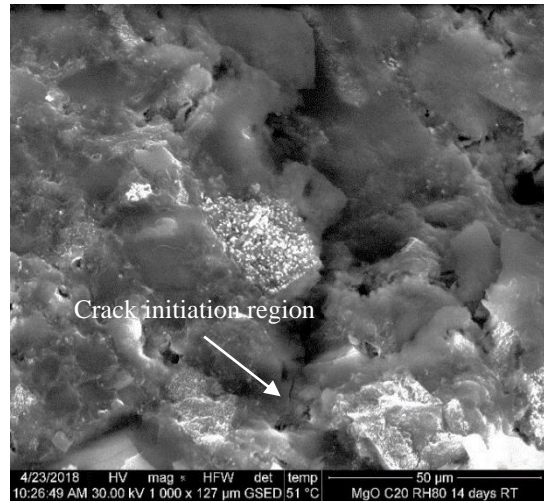


(f)

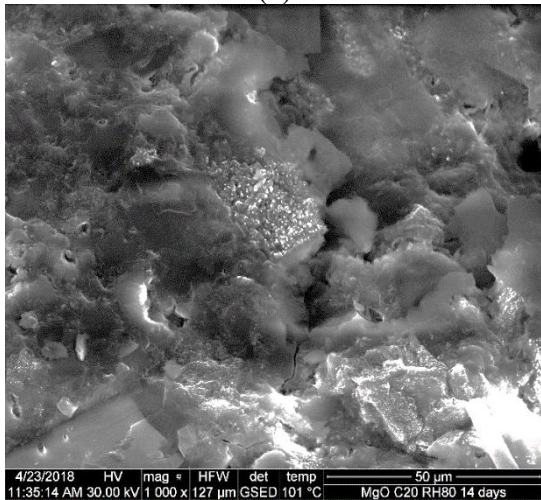
Fig. 4 SEM images of sample after 14 days of 20% CO₂ curing, followed by an exposure to: (a) 30 °C, (b) 50 °C, (c) 100 °C, (d) 200 °C, (e) 300 °C and (f) 400 °C



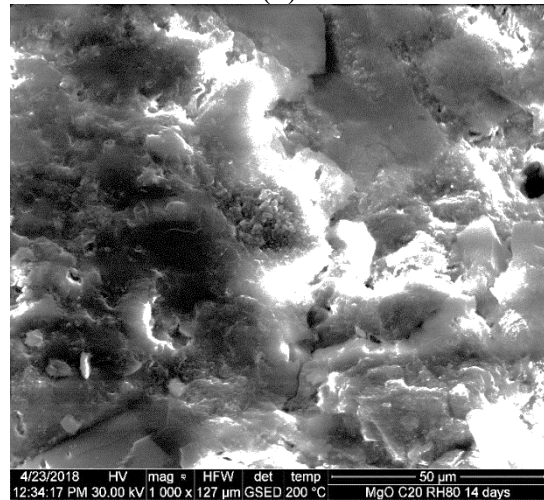
(a)



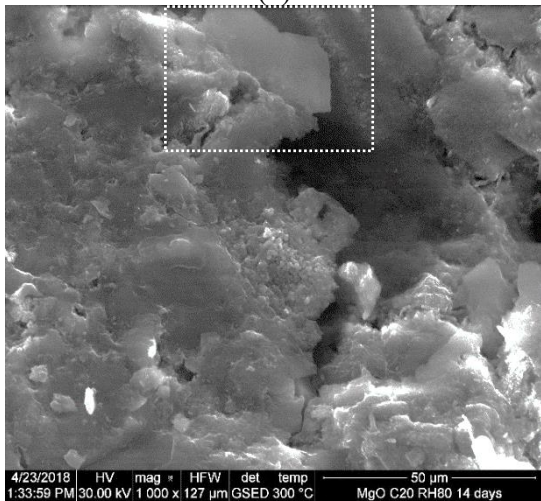
(b)



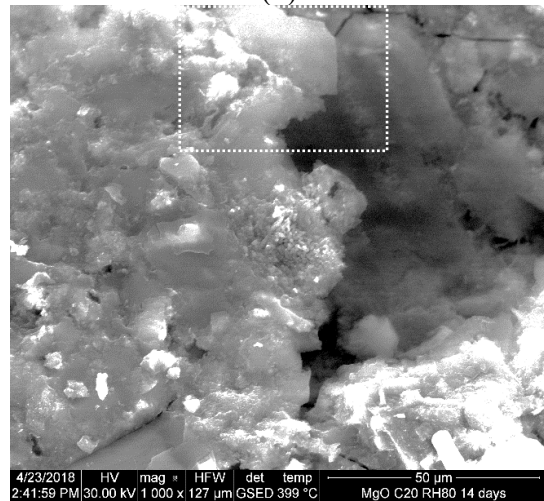
(c)



(d)



(e)



(f)

Fig. 5 ESEM images of 14-day sample cured under 20% CO₂ at different scanning temperatures: (a) 30 °C, (b) 50 °C, (c) 100 °C, (d) 200 °C, (e) 300 °C and (f) 400 °C

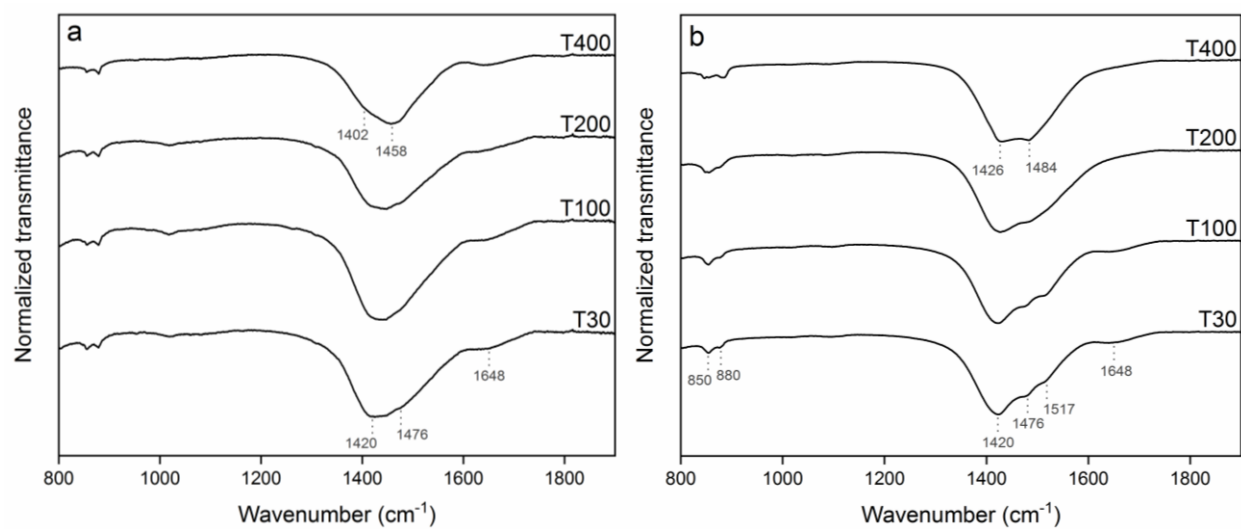
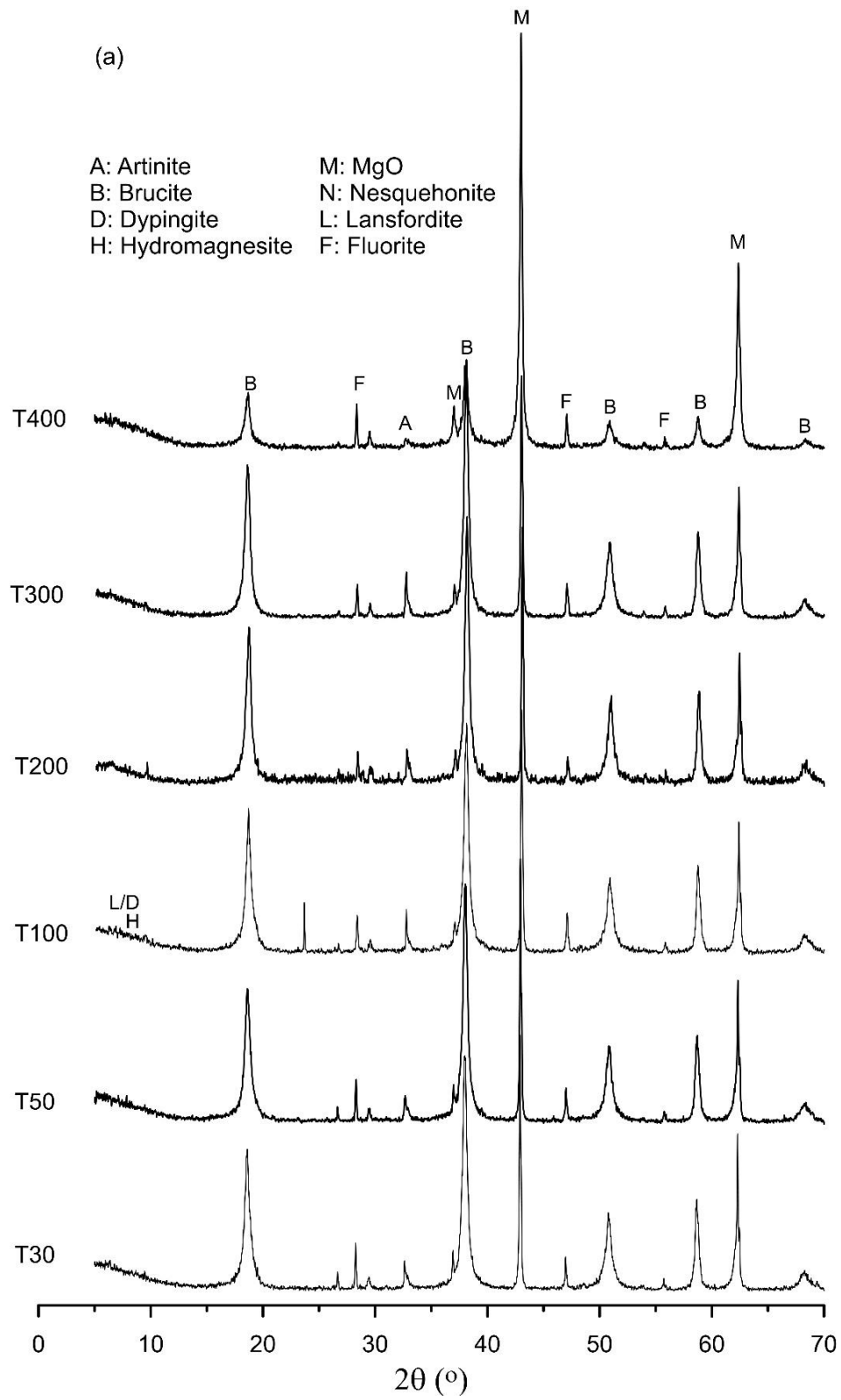


Fig. 6 FTIR spectra of samples cured under (a) ambient and (b) accelerated carbonation conditions heated at different temperatures



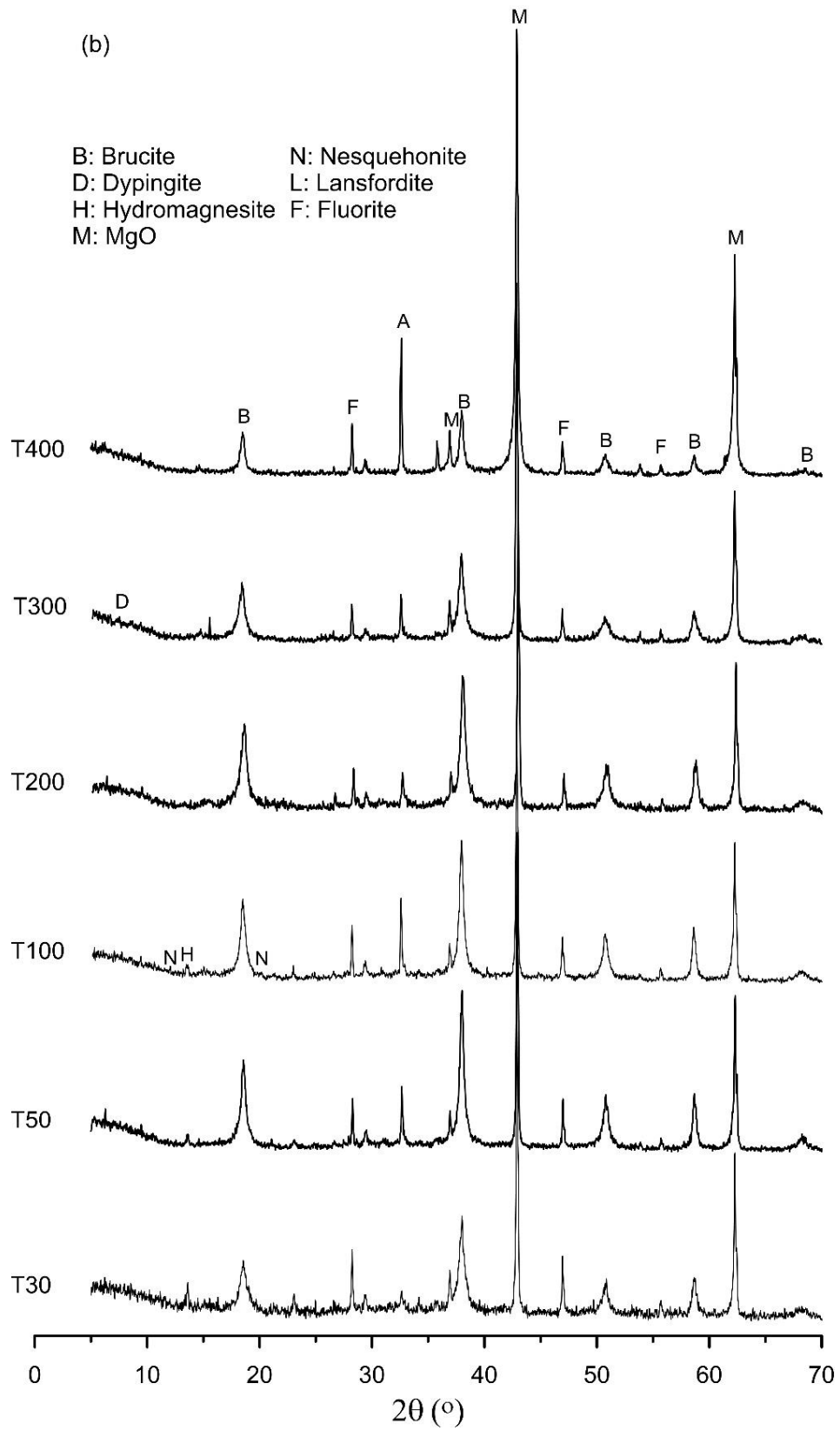


Fig. 7 XRD patterns of concrete samples after heating, cured under: (a) ambient and (b) 20% CO₂ conditions

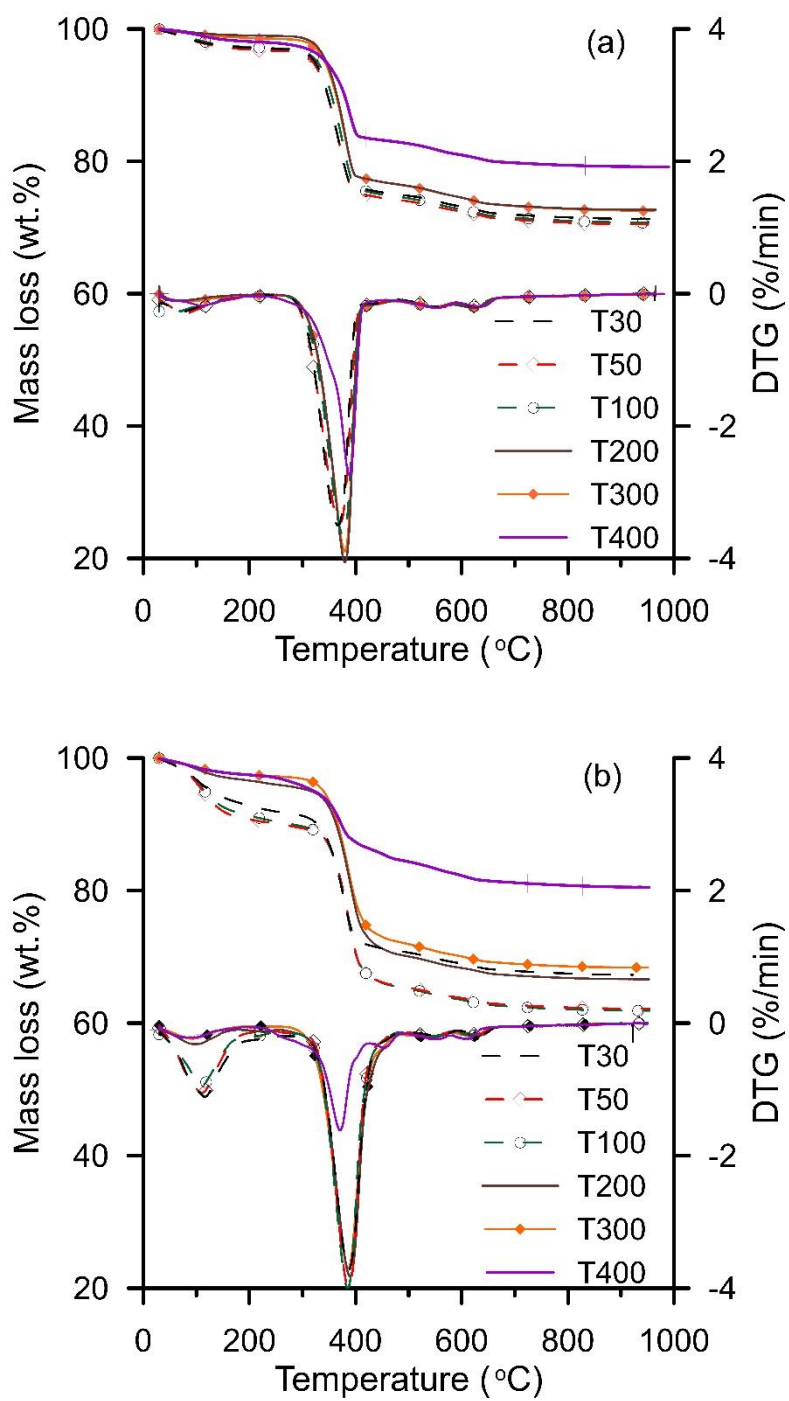


Fig. 8 TGA and DTG of samples after heating, cured under: (a) ambient and (b) 20% CO₂ conditions

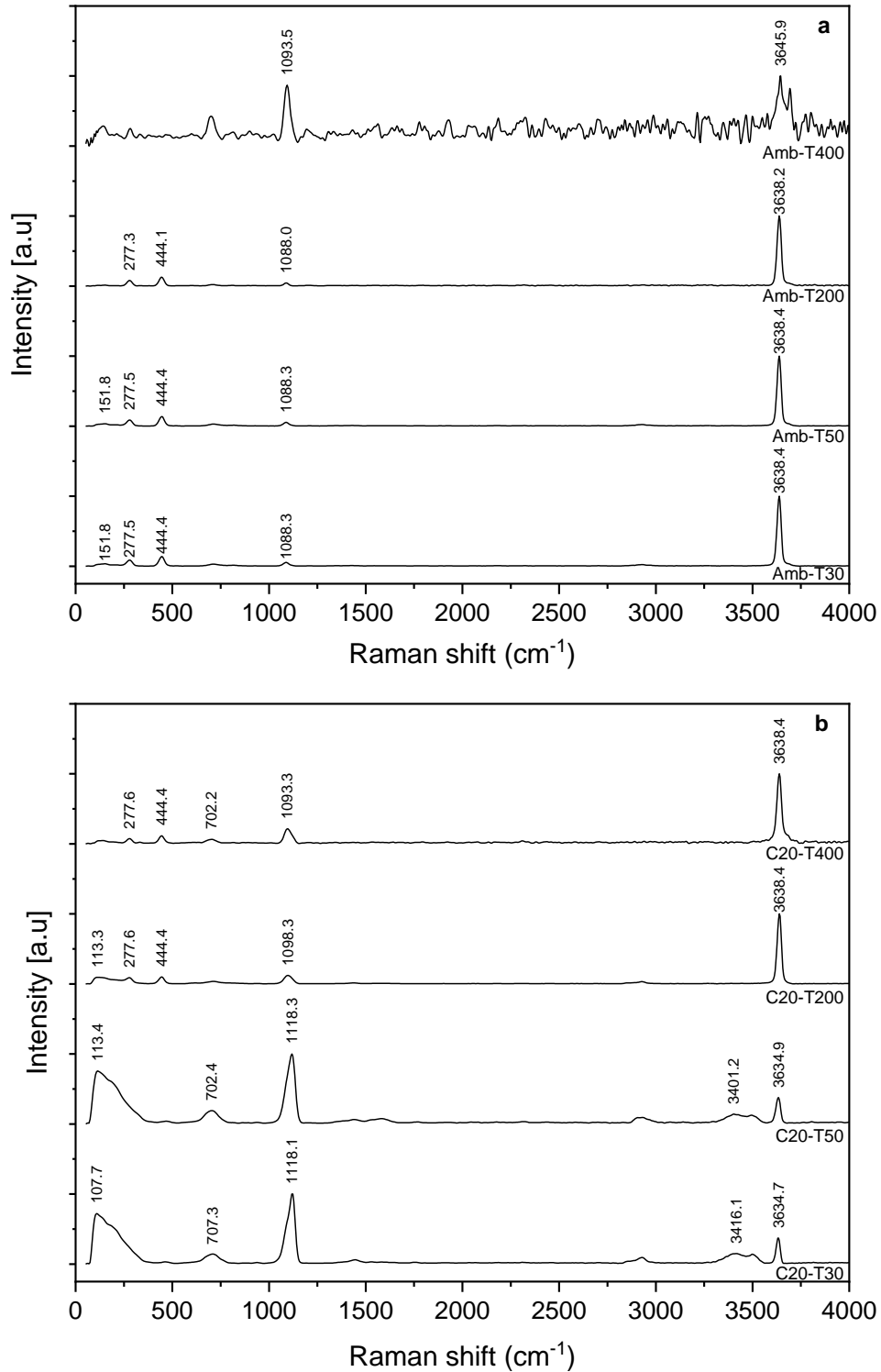


Fig. 9 Raman spectra with 600 g/mm detector of samples cured under (a) ambient and (b) 20% CO₂ conditions and subjected to heating at 30 °C, 50 °C, 200 °C, and 400 °C for 2 hours

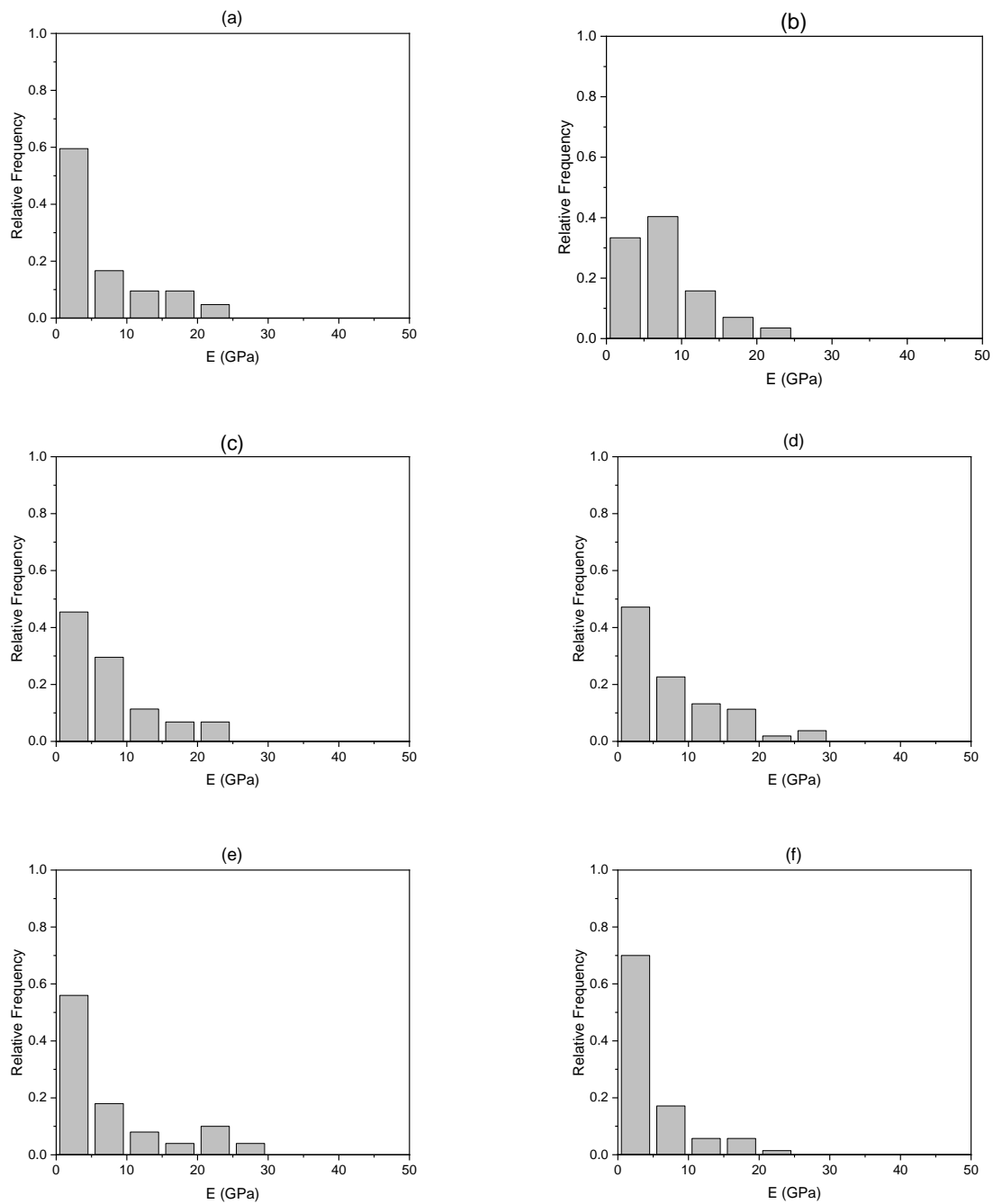


Fig. 10 Nanoindentation results of samples after ambient condition curing, followed by exposure to: (a) 30 °C, (b) 50 °C, (c) 100 °C, (d) 200 °C, (e) 300 °C, and (f) 400 °C

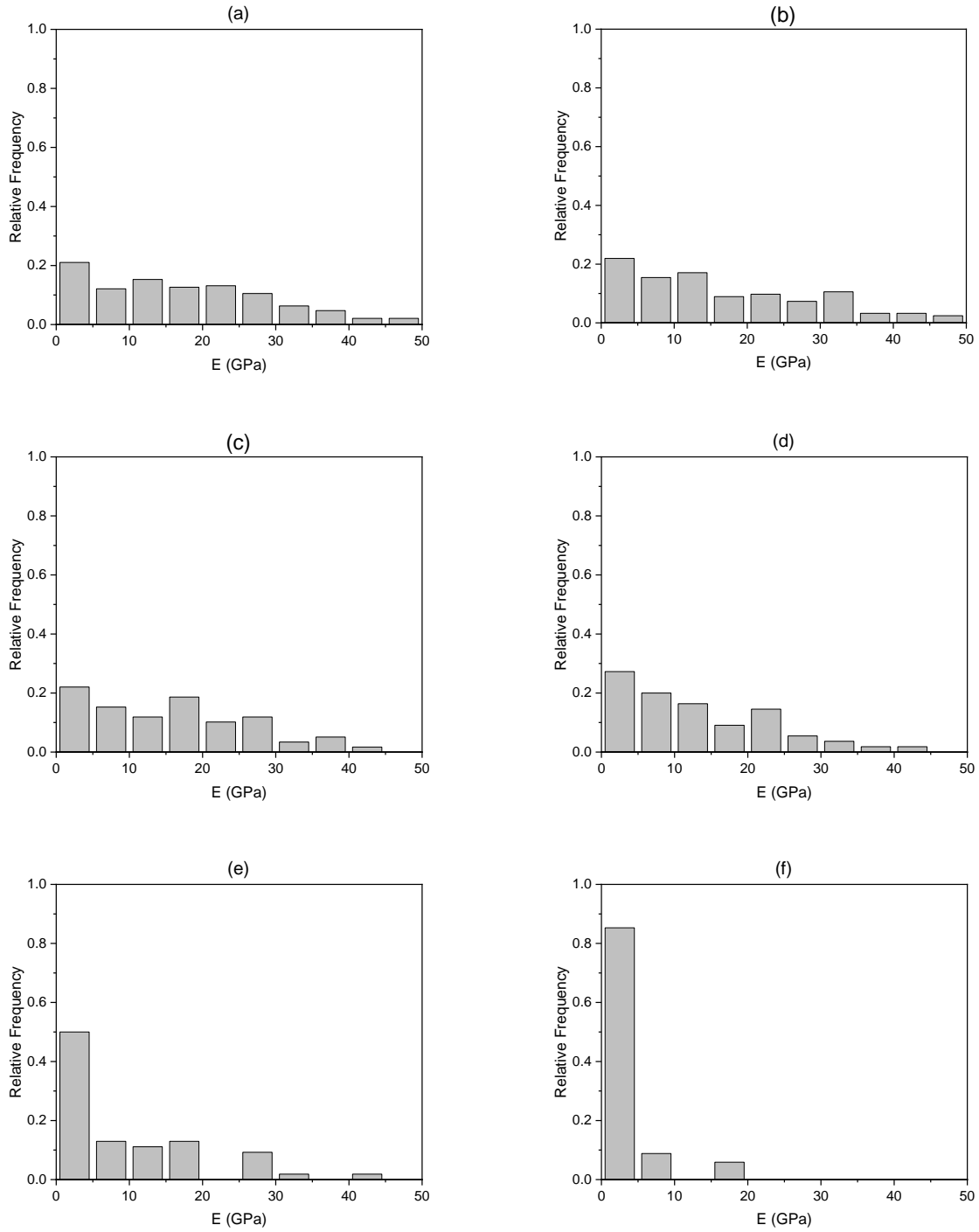


Fig. 11 Nanoindentation results of samples after 14 days of 20% CO_2 curing, followed by exposure to (a) 30 °C, (b) 50 °C, (c) 100 °C, (d) 200 °C, (e) 300 °C, and (f) 400 °C

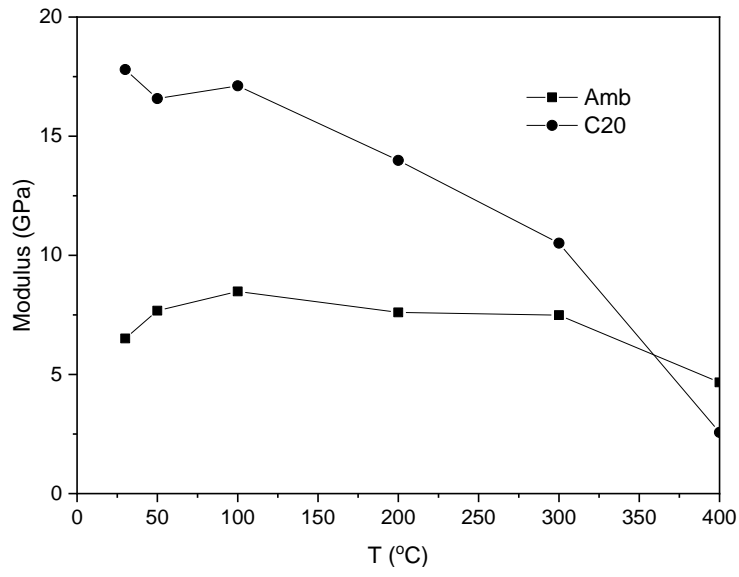


Fig. 12 Average elastic modulus based on the nanoindentation of heated samples after 14 days of curing under ambient and 20% CO₂ conditions